

AD-A265 901



**S** DTIC  
ELECTE  
JUN 18 1993  
**C** **D**



WL-TR-93-3015

**VISCOUS FLOW SIMULATION USING AN UPWIND METHOD  
FOR HEXAHEDRAL BASED ADAPTIVE MESHES**

Michael. J. Aftosmis  
Computational Fluid Dynamics Branch  
Aeromechanics Division

March 1993

Final Report for Period April 1992 - January 1993

Approved for public release; distribution is unlimited

**93-13746**




FLIGHT DYNAMICS DIRECTORATE  
WRIGHT LABORATORY  
AIR FORCE MATERIEL COMMAND  
WRIGHT-PATTERSON AIR FORCE BASE, OHIO 45433-7562

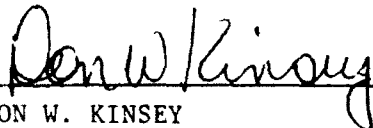
NOTICE

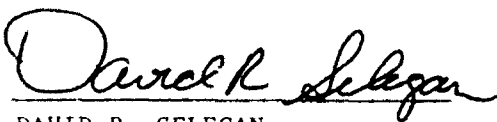
When Government drawings, specifications, or other data are used for any purpose other than in connection with a definitely Government-related procurement, the United States Government incurs no responsibility or any obligation whatsoever. The fact that the government may have formulated or in any way supplied the said drawings, specifications, or other data, is not to be regarded by implication, or otherwise in any manner construed, as licensing the holder, or any other person or corporation; or as conveying any rights or permission to manufacture, use, or sell any patented invention that may in any way be related thereto.

This report is releasable to the National Technical Information Service (NTIS). At NTIS, it will be available to the general public, including foreign nations.

This technical report has been reviewed and is approved for publication.

  
MICHAEL J. AFTOSMIS, Capt, USAF  
Aerodynamicist  
CFD Research Section

  
DON W. KINSEY  
Actg Chief  
CFD Branch

  
DAVID R. SELEGAN  
Chief  
Aeromechanics Division

If your address has changed, if you wish to be removed from our mailing list, or if the addressee is no longer employed by your organization please notify WL/FIMC, WPAFB, OH 45433-7913 to help us maintain a current mailing list.

Copies of this report should not be returned unless return is required by security considerations, contractual obligations, or notice on a specific document.

REPORT DOCUMENTATION PAGE			Form Approved OMB No 0704 0188	
Public reporting burden for this collection of information is estimated to average 1 hour per response, including the time for reviewing instructions, searching existing data sources, gathering and maintaining the data needed, and completing and reviewing the collection of information. Send comments regarding this burden estimate or any other aspect of this collection of information, including suggestions for reducing this burden, to Washington Headquarters Services, Directorate for Information Operations and Reports, 1215 Jefferson Davis Highway, Suite 1204, Arlington, VA 22202-4302, and to the Office of Management and Budget, Paperwork Reduction Project (0704-0188), Washington, DC 20503.				
1. AGENCY USE ONLY (Leave blank)	2. REPORT DATE 1 Mar 93	3. REPORT TYPE AND DATES COVERED Final, April 1992 - January 1993		
4. TITLE AND SUBTITLE Viscous Flow Simulation Using an Upwind Method for Hexahedral Based Adaptive Meshes			5. FUNDING NUMBERS PR: 2404 TA: T5 WU: 00	
6. AUTHOR(S)  Michael J. Aftosmis				
7. PERFORMING ORGANIZATION NAME(S) AND ADDRESS(ES) Flight Dynamics Directorate Wright Laboratory Air Force Materiel Command Wright-Patterson AFB OH 45433-7562			8. PERFORMING ORGANIZATION REPORT NUMBER  WL-TR-93-3015	
9. SPONSORING/MONITORING AGENCY NAME(S) AND ADDRESS(ES) Flight Dynamics Directorate Wright Laboratory Air Force Materiel Command Wright-Patterson AFB OH 45433-7562			10. SPONSORING/MONITORING AGENCY REPORT NUMBER	
11. SUPPLEMENTARY NOTES				
12a. DISTRIBUTION/AVAILABILITY STATEMENT  Approved for public release; distribution is unlimited.			12b. DISTRIBUTION CODE	
13. ABSTRACT (Maximum 200 words) Details of an adaptive, high resolution, upwind algorithm for the simulation of viscous flows on unstructured hexahedral meshes are presented. The method used a TVD scheme for modeling the inviscid terms while the viscous terms rely upon central differencing. Grid adaptation is achieved through directional division of hexahedral cells in response to flow features. The discussion focuses primarily on details of the new viscous discretization and evaluates it through example problems, analysis and mathematical proof. Several issues facing the development of upwind schemes on adaptive, unstructured meshes are prominently discussed. The test cases examine issues of consistency and mesh convergence of the adaptive methodology and the ability of the adaptation to accurately resolve flows which require detailed resolution of subtle flow features. These examples point out several general issues regarding the interaction of the upwind inviscid discretization with the centrally differenced viscous terms, especially near inviscid stagnation points, and within the boundary layer itself. A technique for avoiding the appearance of anomalous solutions in such regions is presented and discussed.				
14. SUBJECT TERMS  Upwind Methods, TVD, Viscous Flows, Unstructured Meshes			15. NUMBER OF PAGES 68	
			16. PRICE CODE	
17. SECURITY CLASSIFICATION OF REPORT Unclassified	18. SECURITY CLASSIFICATION OF THIS PAGE Unclassified	19. SECURITY CLASSIFICATION OF ABSTRACT Unclassified	20. LIMITATION OF ABSTRACT Unlimited	

Accession For	
NTIS CRA&I	<input checked="" type="checkbox"/>
DTIC TAB	<input type="checkbox"/>
Unannounced	<input type="checkbox"/>
Justification	
By	
Distribution /	
Availability Codes	
Dist	Avail and/or Special
A-1	

# Table of Contents

**List of Figures** ..... v

**List of Tables**.....vii

**Acknowledgments**.....viii

**List of Symbols**..... ix

**1. Introduction**..... 1

**2. Description of Method**..... 4

2.1 Governing Equations..... 4

2.2 Spatial Discretization ..... 6

2.3 Discretization Strategy ..... 8

2.4 Unstructured Implementation .....13

2.5 Eigenvalue Scaling for High Aspect Ratio Cells.....17

**3. Adaptation** .....18

3.1 Detection/Division .....18

3.2 Mesh Smoothing.....19

3.3 Geometry Definition.....20

**4. Numerical Experiments and Discussion**.....24

4.1 AGARD 03 Test Case.....24

4.2 Flat Plate Boundary Layer Flow.....	25
4.3 Symmetric Laminar Airfoil Test Case.....	32
4.4 Separation Location.....	38
4.5 Entropy Cutoff and Non-Physical Solutions.....	41
<b>5. Summary and Conclusions .....</b>	<b>45</b>
<b>6. References.....</b>	<b>47</b>
<b>Appendix .....</b>	<b>51</b>

# List of Figures

<b>Figure 1.</b> Formation of dual mesh of <i>Auxiliary Cells</i> in two and three dimensions.....	7
<b>Figure 2.</b> Construction of <i>Secondary Cell</i> for the calculation of first derivatives on the <i>E</i> face of the auxiliary cell surrounding node <i>i</i> . ....	11
<b>Figure 3.</b> Construction of surface vectors on secondary cell around edge $\bar{ij}$ . ....	12
<b>Figure 4.</b> Contribution of physical cell <i>C</i> to the integration of the secondary cell surrounding edge $\bar{ij}$ - the front-south ( <i>fs</i> ) edge of cell <i>C</i> . ....	15
<b>Figure 5.</b> Reconstruction of surface geometry from surface data base.....	21
<b>Figure 6.</b> Triangulated surface geometry and resulting computational mesh after mapping physical cells onto surface. Original mesh consisted of 14x14 cube. 1 smoothing pass, and 1 surface reconstruction sweep. ....	23
<b>Figure 7.</b> Mach contours (inc.=0.05) and adapted upper half mesh for AGARD 03 test case. Mach 0.95, $\alpha = 0^\circ$ , inviscid flow. 18,000 nodes. ....	26
<b>Figure 8.</b> Near field Mach contours (inc.=0.05) for AGARD 03 test case.....	27
<b>Figure 9.</b> Effects of cutting off all or only the nonlinear eigenvalues on flat plate boundary layer simulation using the TVD discretization. Comparison with Blasius similarity solution, $M_\infty = 0.5$ , $Re_L = 5,000$ .....	29
<b>Figure 10.</b> Velocity profiles for flat plate boundary layer solutions using TVD convective discretization and applying the entropy cutoff to all eigenvalues. ....	30
<b>Figure 11.</b> Velocity profiles for flat plate boundary layer solutions using central difference convective discretization with 4th difference artificial dissipation ( $\nu_4$ ). ....	31

<b>Figure 12.</b> Skin friction evolution along flat plate using both Upwind TVD and central differencing. Entropy cutoff applied to all eigenvalues in TVD solutions. Blasius solution provided for comparison. $M_\infty = 0.5$ , $Re_L = 5,000$ .	34
<b>Figure 13.</b> Adapted half-C mesh near airfoil for viscous NACA 0012 test case. 5 levels of cells, 8,100 nodes, $M_\infty = 0.5$ , $Re_c = 5,000$ .	35
<b>Figure 14.</b> Mach contours (inc. = 0.01) in discrete solution using TVD discretization and applying entropy cutoff to all eigenvalues. Separation point at 81.5% chord. $M_\infty = 0.5$ , $Re_c = 5,000$ .	36
<b>Figure 15.</b> $C_p$ and $C_f$ profiles for NACA 0012 at $M_\infty = 0.5$ and $Re_c = 5,000$ . Entropy cutoff applied to all eigenvalues.	37
<b>Figure 16.</b> Velocity vectors and computed streamlines near separation point at trailing edge of airfoil.	39
<b>Figure 17.</b> Variation of separation location with mesh refinement. $\Delta x$ is the mesh spacing in the streamwise direction	40
<b>Figure 18.</b> Stagnation region at leading edge of NACA 0012 after second adaptation.	42

# List of tables

**Table 1.** Separation Locations Predicted by Several Methods..... 38



# Acknowledgments

Computing support for this study was provided by the Phillips Laboratory Supercomputing Center at Kirtland AFB. This support is gratefully acknowledged. The author would like to sincerely thank Drs. D. Gaitonde, M. Visbal and N. Kroll of DLR Braunschweig for their many contributions to this work.

## List of Symbols

$c$	airfoil chord in numerical simulations
$\partial V$	closed boundary of $V$
$e$	total internal energy per unit mass
$\bar{F}$	complete flux density tensor
$L$	reference length of flat plate
$\bar{n}$	unit normal vector $[n_x, n_y, n_z]^T$
$p$	local static pressure
$Pr$	Prandtl number
$\bar{Q}_k$	vector of numerical flux through face $k$
$Re$	Reynolds number
$Rs$	shock refinement parameter
$\bar{S}_k$	surface vector of face $k$ $[S_x, S_y, S_z]^T$
$T$	local static temperature
$\bar{U}$	state vector $[\rho, \rho u, \rho v, \rho w, e]^T$
$u, v, w$	Cartesian velocity components $x_1, x_2, x_3$
$V_i$	volume of cell $i$
$\delta$	small parameter preventing zero wave speed, $\delta \ll 1$
$\eta$	free index, 1, 2, 3, or 4
$\phi_\eta$	element of vector $[u, v, w, T]^T$
$\lambda$	eigenvalue of flux Jacobian matrix
$\rho$	density
$\xi$	free index, 1, 2, or 3
$d_\xi \phi_\eta$	tensor of first derivatives

# 1. Introduction

The recent success of characteristic based upwind differencing on structured meshes has spurred significant interest into adopting such methods into unstructured adaptive mesh algorithms<sup>[1],[2],[3]</sup>. Both adaptation and upwind differencing strive to increase the accuracy and efficiency of the numerical simulation, and the combination of the two approaches suggests a powerful and flexible platform for the simulation of flows with features spanning a wide spectrum of length scales.

Adaptive mesh methods and upwind techniques were both developed and tested on inviscid flow problems, and it may be convincingly argued that some aspects of their application to multi-dimensional viscous flow remain incompletely understood. Most successful upwind techniques, for example, rely upon the solution of a Riemann problem on a direction-by-direction basis<sup>[3]</sup>. The spatial operator resulting from this approach cannot be considered truly isotropic and its interaction with the viscous discretization (often central difference) has not been extensively researched. Moreover, in viscous dominated regions, the Riemann problem solved by the convective discretization becomes ill-posed due to the presence of large viscous terms in the governing equations. Nevertheless, the overwhelming success of upwind methods at providing high quality solutions to complex flows continues to motivate considerable research into these and other fundamental topics<sup>[4],[5]</sup>.

Unstructured, adaptive, mesh methods have enjoyed a similar degree of success in the last decade. From their initial application to inviscid 2D flows<sup>[6],[7],[8]</sup>, through complete three dimensional simulations over complex geometries<sup>[9],[10],[11]</sup>, such techniques have promised outstanding efficiency by clustering mesh nodes where they are most needed in the evolving solution. Nevertheless, several outstanding issues still exist. Credible and general techniques for deciding where to adapt the solution have yet to be definitively determined, and fundamental questions exist concerning mesh convergence and consistency<sup>[12]</sup>. Current research efforts are also focusing ever more sharply on issues of mesh quality and the local disruption of mesh metrics caused by introducing new nodes into the computational domain<sup>[13],[14]</sup>. The issue of mesh quality is of particular importance in the discretization of the viscous terms in the full Navier-Stokes equations. The second differences in such terms are computed as the first difference of first differences, thus compounding mesh stretching or skewing errors and resulting in much more stringent requirements on mesh or element quality. This problem is further compounded by the highly nonlinear nature of viscous flow which increases the importance of resolving subtle flow features which may be very readily disturbed by mesh irregularity. As a result, conclusive demonstration of adaptive unstructured mesh techniques in resolving fine detail within an adapted flow field remains elusive.

Recently, an upwind based solver for the 3D Navier-Stokes equations was introduced<sup>[15]</sup>. The method uses adaptively refined hexahedral based meshes and permits adaptation through directional cell division. Such cells provide a natural environment for mapping the multi-dimensional upwind stencil which relies on 1D operators in each spatial direction. Additionally, the tessellation easily forms the high quality surface mesh required for accurate evaluation of the stress tensor and heat flux vector.

This report focuses on the viscous aspects of the technique and includes a detailed presentation of the discretization and implementation of these terms. This includes a discussion of the order of accuracy and its degeneration on nonuniform meshes. It also includes an examination of

several basic numerical properties designed into the scheme. A section addressing mesh smoothness and surface point introduction is also included. Various sub- and transonic example problems facilitate a discussion of the topics mentioned in the preceding paragraphs. These examples also provide a basis for examining the interaction of the upwind scheme with the centrally differenced viscous terms - especially within the boundary layer itself and near regions where the entropy condition<sup>[16]</sup> may be violated.

## 2. Description of Method

### 2.1 Governing Equations

The Navier-Stokes equations describing the unsteady flow of a viscous perfect gas may be written in integral form:

$$\iiint_V \frac{\partial \bar{U}}{\partial t} dV = - \oint_{\partial V} \bar{\bar{F}} \cdot \bar{n} ds \quad (1)$$

$$\bar{\bar{F}} \equiv \bar{\bar{F}}_I - \bar{\bar{F}}_V \quad (2)$$

Here  $\bar{U}$  is the state vector of conserved variables, and  $\bar{\bar{F}}$  is the complete tensor of flux density which contains both inviscid and viscous components.  $V$  refers to an arbitrary control volume and  $\partial V$  is its closed boundary with the outward facing unit vector  $\bar{n} = [n_x, n_y, n_z]^T$ . In Eqs.(1) and (2):

$$\bar{U} = \begin{bmatrix} \rho \\ \rho u \\ \rho v \\ \rho w \\ \rho E \end{bmatrix}; \quad \bar{\bar{F}}_I = \begin{bmatrix} \rho u i & + & \rho v j & + & \rho w k \\ (\rho u^2 + p)i & + & \rho u v j & + & \rho u w k \\ \rho u v i & + & (\rho v^2 + p)j & + & \rho v w k \\ \rho u w i & + & \rho v w j & + & (\rho w^2 + p)k \\ (\rho u E + u p)i & + & (\rho v E + v p)j & + & (\rho w E + w p)k \end{bmatrix}; \quad (3)$$

$$\bar{\bar{F}}_V = \begin{bmatrix} 0i + 0j + 0k \\ \tau_{xx}i + \tau_{xy}j + \tau_{xz}k \\ \tau_{yx}i + \tau_{yy}j + \tau_{yz}k \\ \tau_{zx}i + \tau_{zy}j + \tau_{zz}k \\ \Pi_x i + \Pi_y j + \Pi_z k \end{bmatrix}; \text{ where } \begin{aligned} \Pi_x &= u\tau_{xx} + v\tau_{xy} + w\tau_{xz} - q_x \\ \Pi_y &= u\tau_{yx} + v\tau_{yy} + w\tau_{yz} - q_y \\ \Pi_z &= u\tau_{zx} + v\tau_{zy} + w\tau_{zz} - q_z \end{aligned}$$

In this work, the equation of state for a calorically perfect gas relates the mechanical and thermodynamic properties of the fluid

$$p = (\gamma - 1) \left( \rho E - \frac{\rho V^2}{2} \right) \quad (4)$$

The viscous part of the flux density tensor makes use of the shear stress tensor and heat flux vector. These are modeled by adopting the Stokes Hypothesis, while assuming an isotropic, Newtonian fluid yields a symmetric shear stress tensor.

$$\begin{aligned} \tau_{xx} &= 2\mu u_x - \frac{2}{3}\mu(u_x + v_y + w_z) & q_x &= -k \frac{\partial T}{\partial x} \\ \tau_{yy} &= 2\mu v_y - \frac{2}{3}\mu(u_x + v_y + w_z) & q_y &= -k \frac{\partial T}{\partial y} \\ \tau_{zz} &= 2\mu w_z - \frac{2}{3}\mu(u_x + v_y + w_z) & q_z &= -k \frac{\partial T}{\partial z} \\ \tau_{xy} &= \tau_{yx} = \mu(u_y + v_x) \\ \tau_{xz} &= \tau_{zx} = \mu(u_z + w_x) \\ \tau_{yz} &= \tau_{zy} = \mu(v_z + w_y) \end{aligned} \quad (5)$$

Sutherland's law approximates the fluctuation of molecular viscosity with temperature.

$$\mu = \frac{1}{Re} \left[ \frac{T_\infty + 110.4}{T + 110.4} \right] \left( \frac{T}{T_\infty} \right)^{\frac{3}{2}} \quad (T \text{ in Kelvin}) \quad (6)$$

Finally, the Prandtl number relates the thermal conductivity to viscosity.

$$k = \frac{1}{\gamma - 1} \frac{\mu}{Pr} \quad (7)$$

## 2.2 Spatial Discretization

The discretization of these equations may be conveniently developed by focusing on the symbolic form of the governing equations given in expression {1}. Considering a control volume fixed in time and applying the mean value theorem, this equation may be recast as:

$$\left(\frac{\partial \bar{U}}{\partial t}\right)_V = -\frac{1}{V} \oint_{\partial V} \bar{\mathbf{F}} \cdot \bar{\mathbf{n}} ds \quad (8)$$

Equation {8} may be further specialized for application to a specific polyhedral control volume, constructed, with planar faces, around node  $i$  (Fig. 1). Equation {8} may then be approximated by:

$$\frac{\partial \bar{U}_i}{\partial t} = -\frac{1}{V_i} \sum_{k \in \partial V_i} \bar{\mathbf{F}}_I^k \cdot \bar{\mathbf{S}}^k + \frac{1}{V_i} \sum_{k \in \partial V_i} \bar{\mathbf{F}}_V^k \cdot \bar{\mathbf{S}}^k \quad (9)$$

where  $k$  denotes the  $k^{th}$  face of  $V_i$ ,  $\bar{\mathbf{S}}^k = [s_x^k, s_y^k, s_z^k]^T$  is the surface vector of face  $k$ . The first term on the RHS of Eq.(9) performs the inviscid surface integral while the second term balances the viscous fluxes through the faces of  $V_i$ .

The solution method separates the modeling of convective and viscous fluxes. It uses an upwind representation of the inviscid fluxes, while the viscous fluxes utilize central differencing. The convective modeling has been extensively documented and Refs. [17], [2], and Ref. [19] contain details of its formulation and validation. Ref. [20] contains structured mesh results demonstrating the exceptional shock capturing properties of this formulation, while Ref. [21] demonstrates that this inviscid discretization also accurately represents smooth features with a low level of background diffusion (as compared to both central and other upwind methods). Ref. [2] focuses solely on the unstructured implementation of this method and shows that the properties associated with this scheme on a structured mesh are retained in the unstructured procedure. Additionally, the inviscid discretization has a central difference option using the



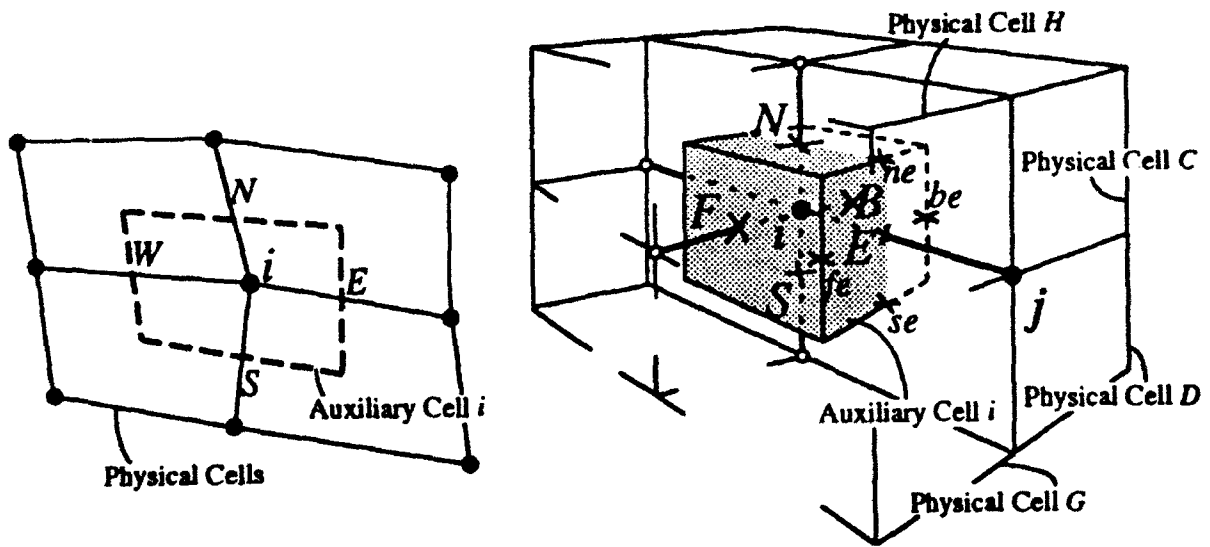


Figure 1. Formation of dual mesh of Auxiliary Cells in two and three dimensions.

blended 2<sup>nd</sup> and 4<sup>th</sup> order artificial dissipation from Ref. [22]. This permits a direct comparison of upwind and central results on identical adapted meshes.

The integration of both inviscid and viscous fluxes proceeds on a dual mesh formed by connecting the geometric centers of the cells of the physical mesh. Figure 1 illustrates the formation of this dual, *auxiliary mesh*, in two and three dimensions. The inviscid and viscous fluxes are balanced through the faces of the auxiliary cells resulting in a node-based method which promotes accurate and straightforward treatment of boundaries. Evaluating the summations of Eq.(9) then forms an update of the state vector at each node through a multi-stage Runge-Kutta time integration scheme.

### 2.3 Discretization Strategy

As suggested by the form of Eq.(9), the complete update to any node,  $\Delta \bar{U}_i$ , is a summation of inviscid and viscous contributions.

$$\Delta \bar{U}_i = (\Delta \bar{U}_i)_I + (\Delta \bar{U}_i)_V \quad (10)$$

The choice of central differencing for the viscous fluxes allows the scheme to be written extremely compactly. Eventually it involves only node-to-cell and cell-to-node communication while organizing all gather-scatter operations so that they may be easily grouped for rapid processing. These communication issues remain important because the current implementation uses a cell based data structure and each physical cell can address only the nodes at its vertices directly[6],[23]. Thus, an implementation based upon cell-to-node operations is especially convenient.

It is worth noting that this basic discretization is also amenable to edge-based data structures. In fact, Ref. [24] describes the formulation of Hessian and Laplacian operators using only edge-based formulas. For the hexahedral based meshes discussed here, however, this strategy holds little obvious advantage, and the cell-based formulas were used.

In two dimensions, the viscous discretization degenerates into a form which is conceptually similar to that first presented by Ref. [23]. The current work contains some important differences in the handling of surface vectors, time steps, and volumes, however, and the extension to three dimensions is completely new.

Figure 1 contains a view of the cells surrounding node  $i$  in two and three dimensions. The stress tensor and viscous fluxes are computed on each of the faces ( $N, S, E, W, F, B$ ) of auxiliary cell  $i$  to form its viscous update  $\Delta \bar{U}_{Visc}$ .

$$\Delta \bar{U}_{Visc} = \frac{\Delta t}{V} \sum_{k \in \partial V} \bar{F}_V^k \cdot \bar{S}^k$$

Applying the mid-point rule for integration and suppressing the subscript ( $v$ ) for compactness:

$$\Delta \bar{U}_{Visc} = \frac{\Delta t}{V} [ \bar{F}^N \cdot \bar{S}^N - \bar{F}^S \cdot \bar{S}^S + \bar{F}^E \cdot \bar{S}^E - \bar{F}_i^W \cdot \bar{S}^W + \bar{F}^F \cdot \bar{S}_i^F - \bar{F}^B \cdot \bar{S}^B ] \quad (11)$$

The superscripts in Eq.(11) refer to the face associated with each quantity, and thus  $\bar{S}^N$  is the surface vector of the North face of the auxiliary cell surrounding node  $i$ . The sign convention used takes the Cartesian components of the surface vectors as positive when oriented in positive coordinate directions. These surface vectors are also necessary for the inviscid integration and are computed only once.

Each of the viscous fluxes in Eq.(11) is constructed through a linear combination of elements of the shear stress tensor (see Eqs.(3) and (5)). Filling this tensor requires spatial derivatives of velocity and temperature. These derivatives may be conveniently expressed in tensor notation by defining the free index  $\xi = 1, 2, \text{ or } 3$  and denoting the  $x, y, z$  axes as  $x_1, x_2, \text{ and } x_3$ .  $\partial(\ ) / \partial x_\xi = d_\xi(\ )$  denotes partial differentiation with respect to the coordinate directions. Taking a second free index  $\eta = 1, 2, 3, \text{ or } 4$ , the vector  $\bar{\phi}$  may be defined as  $\bar{\phi} = [u, v, w, T]^T$ , any element of which may be referred to as  $\phi_\eta$ . With these conventions, the complete set of first derivatives needed to fill the shear stress tensor may be denoted as simply  $d_\xi \phi_\eta$ .

$$d_{\xi}\phi_{\eta} = \begin{bmatrix} \frac{\partial u}{\partial x} & \frac{\partial v}{\partial x} & \frac{\partial w}{\partial x} & \frac{\partial T}{\partial x} \\ \frac{\partial u}{\partial y} & \frac{\partial v}{\partial y} & \frac{\partial w}{\partial y} & \frac{\partial T}{\partial y} \\ \frac{\partial u}{\partial z} & \frac{\partial v}{\partial z} & \frac{\partial w}{\partial z} & \frac{\partial T}{\partial z} \end{bmatrix}; \quad \text{where} \quad \begin{array}{l} \xi = 1, 2, \text{ or } 3 \\ \eta = 1, 2, 3, \text{ or } 4 \end{array} \quad (12)$$

These derivatives must be computed on all the faces of each auxiliary cell, and they are evaluated by taking surface integrals over the *secondary cells* which surround the centers of the faces of auxiliary cells. Figure 2 illustrates the construction of one such secondary cell for the East face of auxiliary cell  $i$  in two and three dimensions.

Each face of the auxiliary cell is uniquely associated with one of the edges incident upon node  $i$ . Thus, the bracket in Eq. (11) contains one term for every edge which terminates at  $i$ , and we actually seek to evaluate  $d_{\xi}\phi_{\eta}$  on the midpoint of each edge in the physical mesh. This point becomes increasingly important when considering more general polyhedral control volumes (i.e. at interfaces of adapted regions, or in meshes composed of nonhexahedral cells). This observation makes obvious the fact that exactly one secondary cell surrounds each edge of the physical mesh. Furthermore, construction of the surface vectors for the secondary cells is now very convenient, since they may be obtained through simple averaging of those associated with the auxiliary cells at either end of the edge. This construction requires only one addition, and one multiplication per face and never more than edge-to-node communication. Figure 3 illustrates the formation of the East secondary cell around edge  $\bar{ij}$ . The proof in the Appendix shows that this construction will always result in closed polyhedra.

With the secondary cells defined, Gauss' Theorem provides an expression for the first derivatives,  $d_{\xi}\phi_{\eta}$ , along all edges of the physical mesh.

$$d_{\xi}\phi_{\eta} = \frac{\partial(\phi_{\eta})}{\partial x_{\xi}} = \frac{1}{V} \oint_{\partial V} \phi_{\eta} n_{\xi} ds \quad (13)$$

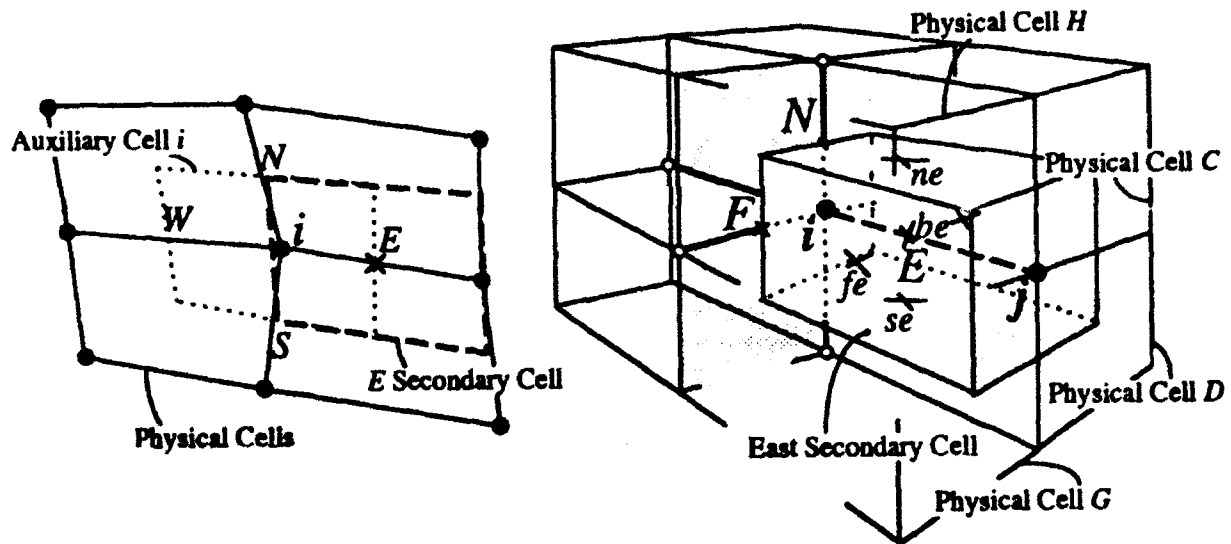
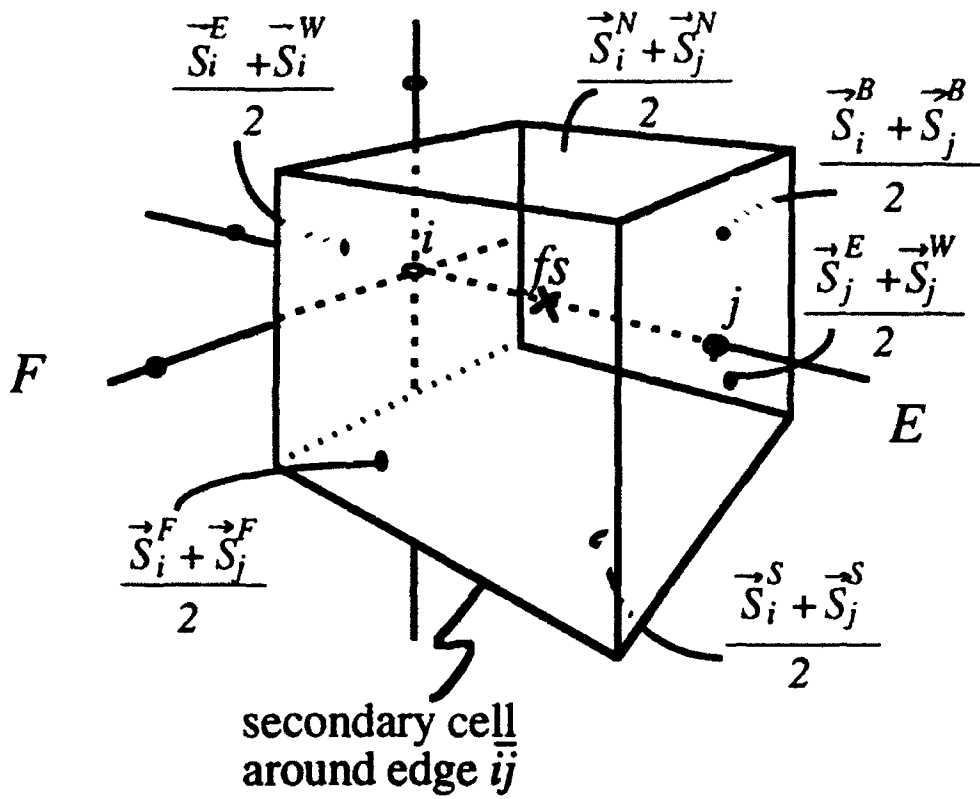


Figure 2. Construction of *Secondary Cell* for the calculation of first derivatives on the *E* face of the auxiliary cell surrounding node *i*.



**Figure 3.** Construction of surface vectors on secondary cell around edge  $ij$ .

where  $n_{\xi}$  is a component of the outward facing normal vector of unit length, and the volume is that of the secondary cell. For the secondary cell surrounding edge  $\bar{ij}$  in Figure 2 this becomes:

$$d_{\xi}\phi_{\eta} = \frac{1}{2} \frac{1}{V} \left[ \begin{aligned} &+ \phi_{\eta}^j (S_{\xi j}^E + S_{\xi j}^W) - \phi_{\eta}^i (S_{\xi i}^E + S_{\xi i}^W) \\ &+ \phi_{\eta}^{ne} (S_{\xi i}^N + S_{\xi j}^N) - \phi_{\eta}^{se} (S_{\xi i}^S + S_{\xi j}^S) \\ &+ \phi_{\eta}^{fe} (S_{\xi i}^F + S_{\xi j}^F) - \phi_{\eta}^{be} (S_{\xi i}^B + S_{\xi j}^B) \end{aligned} \right] \quad \{14\}$$

The superscripts on  $\phi_{\eta}$  refer to the location at which the scalars are evaluated (from Fig. 2). Similar expressions may be constructed on the other edges incident on node  $i$  which facilitate the formation of the viscous fluxes at all faces of the auxiliary cell surrounding node  $i$  and, ultimately, the evaluation of Eq. {11} for  $\Delta U_{Visc}$  at  $i$ .

Since it is based on standard second-order central differencing, the discretization formally retains this order of accuracy on smooth meshes. Furthermore, Ref. [23] shows that, in 2D, the overlapping secondary cells results in a discretization which is capable of recognizing and damping saw-tooth oscillations in the solution. Finally, the Appendix demonstrates that the current choice of auxiliary and secondary control volumes results in an integration which preserves a zero gradient flow on any arbitrary, nonoverlapping mesh (preserves free stream flow).

## 2.4 Unstructured Implementation

An examination of the basic viscous discretization outlined in Eqs. {11} and {14} reveals that it involves only the cells and nodes immediately adjacent to node  $i$ . Furthermore, these are simply central differences and the whole procedure may be divided into a sequence of steps - with no single step requiring more than nearest neighbor communication. The goal of this section is to isolate the contribution of a particular physical cell to the viscous stencils of each of its vertices. This will permit the formation of the viscous updates at all mesh nodes by a single sweep through the physical mesh cells.

Integration of the secondary cell surrounding edge  $\vec{ij}$  requires operations in physical cells  $C$ ,  $D$ ,  $G$ , and  $H$  to provide  $d_{\xi}\phi_{\eta}$  on the East face of the auxiliary cell around node  $i$ . Figure 4 highlights the portion of the integration (in Eq.(14)) contributed to by cell  $C$ . The other physical cells surrounding this edge,  $D$ ,  $G$ , and  $H$ , contribute to this surface integral in a similar fashion. Assuming the volumes of the physical cells are all nearly equal permits isolation of the contribution of physical cell  $C$  to the tensor of first derivatives  $d_{\xi}\phi_{\eta}$  along edge  $ij$ .

Assume  $V_C = V_D = V_G = V_H = V$

$$\begin{aligned}
 (d_{\xi}\phi_{\eta})_C^s = \frac{1}{2V} & \left[ + \frac{\phi_{\eta}^i(S_{\xi_j^E} + S_{\xi_j^W})}{4} - \frac{\phi_{\eta}^i(S_{\xi_i^E} + S_{\xi_i^W})}{4} \right. \\
 & + 0 - \frac{\phi_{\eta}^{se}(S_{\xi_i^S} + S_{\xi_j^S})}{2} \\
 & \left. + \frac{\phi_{\eta}^{fe}(S_{\xi_i^F} + S_{\xi_j^F})}{2} - 0 \right] \quad (15)
 \end{aligned}$$

This edge is the front-south ( $fs$ ) edge of physical cell  $C$  and the notation  $(d_{\xi}\phi_{\eta})_C^s$  reads as "the contribution to  $d_{\xi}\phi_{\eta}$  on the front-south edge of physical cell  $C$ ." Figs. 1 and 2 identify the locations referred to by the superscripts on  $\phi$ , while Fig. 4 helps to clarify the edge labels of the physical cells. The zeros left in this equation facilitate direct comparison with Eq.(14) and the approximation preceding Eq.(15) is necessary to separate out the individual contribution from the cells which border edge  $\vec{ij}$ . This approximation becomes exact on uniform meshes, and on sufficiently fine smooth meshes, so it does not alter the formal second-order accuracy of the method. On stretched meshes, one may show that the additional truncation error created by this approximation is  $O(\Delta x^2)$  and is smaller than the first order error created by the mesh stretching itself.

In the same manner that cell  $C$  contributes to a portion of the secondary cell integration of node  $i$ , it also contributes to a part of the integration of the viscous fluxes on the auxiliary cell around  $i$  (Eq.(11)). After some algebraic manipulation,  $C$ 's role in the flux balance of auxiliary cell  $i$  may be isolated. Since this expression involves the complete viscous part of the flux density



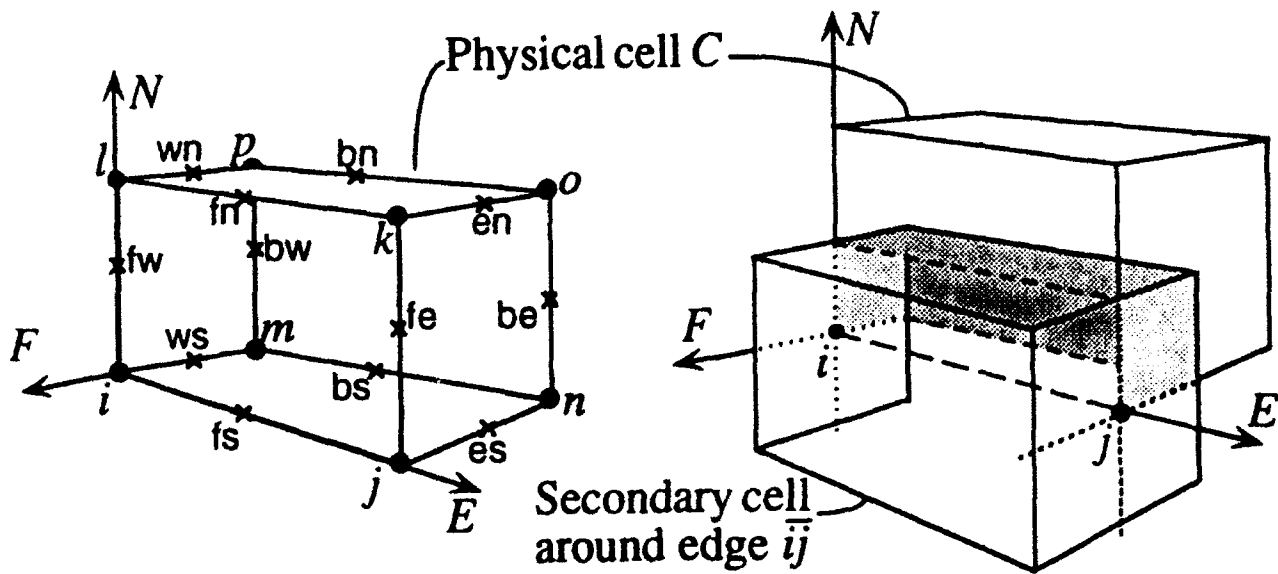


Figure 4. Contribution of physical cell  $C$  to the integration of the secondary cell surrounding edge  $\bar{i}\bar{j}$  - the front-south ( $fs$ ) edge of cell  $C$ .

tensor (denoted by simply  $\bar{F}$  for compactness), it is most convenient to express it using the symbolic form of the notation used previously:

$$(\bar{U}_{visc})_i = \frac{\Delta t_i}{V_i} [\bar{F}_C^{fw} \cdot \bar{S}_i^N + \bar{F}_C^{fs} \cdot \bar{S}_i^E - \bar{F}_C^{ws} \cdot \bar{S}_i^B] \quad (16)$$

The surface vectors on the right of this expression refer to the faces of the auxiliary cell around  $i$  since this is the cell being integrated, and the superscripts and subscripts on  $\bar{F}$  retain their use from the previous equation.  $\bar{F}_C^{fs}$  represents the contribution from cell  $C$  to the viscous part of the flux density tensor along cell  $C$ 's front-south edge. The bracket on the right of Eq.(16) contains three terms - one for each edge of cell  $C$  which is incident upon node  $i$ . As these expressions are applied to nonhexahedral control volumes, this property is retained.

Eq.(16) is really a *Distribution Formula* - in the cell-vertex sense. That is, it contains a contribution from all operations within cell  $C$  that apply to the viscous update at node  $i$ . All these operations are performed completely and without duplication within cell  $C$ , and they are then distributed to node  $i$ . When this node accumulates all the distributions from its surrounding cells, the complete viscous discretization stencil forms. Moreover, information requests are restricted to cell-to-node or node-to-cell inquiries.

In a similar manner, all the physical cells contribute to each of their vertices. The complete set of distribution formulae for a hexahedral cell such as  $C$  are:

$$\begin{aligned} (\Delta \bar{U}_{visc})_{Ci} &= \frac{\Delta t_i}{V_i} (+ \bar{F}_C^{fw} \cdot \bar{S}_i^N + \bar{F}_C^{fs} \cdot \bar{S}_i^E - \bar{F}_C^{ws} \cdot \bar{S}_i^B) \\ (\Delta \bar{U}_{visc})_{Cj} &= \frac{\Delta t_j}{V_j} (- \bar{F}_C^{fs} \cdot \bar{S}_j^w - \bar{F}_C^{es} \cdot \bar{S}_j^B + \bar{F}_C^{ef} \cdot \bar{S}_j^N) \\ (\Delta \bar{U}_{visc})_{Ck} &= \frac{\Delta t_k}{V_k} (- \bar{F}_C^{en} \cdot \bar{S}_k^B - \bar{F}_C^{fn} \cdot \bar{S}_k^w - \bar{F}_C^{fe} \cdot \bar{S}_k^S) \\ (\Delta \bar{U}_{visc})_{Cl} &= \frac{\Delta t_l}{V_l} (+ \bar{F}_C^{fn} \cdot \bar{S}_l^E - \bar{F}_C^{fw} \cdot \bar{S}_l^S - \bar{F}_C^{wn} \cdot \bar{S}_l^B) \end{aligned} \quad (17)$$

$$\begin{aligned}
(\Delta \bar{U}_{visc C})_m &= \frac{\Delta t_m}{V_m} (+ \bar{F}_C^{vs} \cdot \bar{S}_m^F + \bar{F}_C^{bs} \cdot \bar{S}_m^E + \bar{F}_C^{bw} \cdot \bar{S}_m^N) \\
(\Delta \bar{U}_{visc C})_n &= \frac{\Delta t_n}{V_n} (- \bar{F}_C^{bs} \cdot \bar{S}_n^W + \bar{F}_C^{be} \cdot \bar{S}_n^N + \bar{F}_C^{es} \cdot \bar{S}_n^E) \\
(\Delta \bar{U}_{visc C})_o &= \frac{\Delta t_o}{V_o} (- \bar{F}_C^{be} \cdot \bar{S}_o^S - \bar{F}_C^{bn} \cdot \bar{S}_o^W + \bar{F}_C^{en} \cdot \bar{S}_o^F) \\
(\Delta \bar{U}_{visc C})_p &= \frac{\Delta t_p}{V_p} (+ \bar{F}_C^{bn} \cdot \bar{S}_p^E + \bar{F}_C^{wn} \cdot \bar{S}_p^F - \bar{F}_C^{bw} \cdot \bar{S}_p^S)
\end{aligned}$$

When these expressions are evaluated in all the physical cells of the domain, the complete viscous update is formed at all the nodes.

## 2.5 Eigenvalue Scaling for High Aspect Ratio Cells

Near wall boundaries, high aspect ratio cells are commonly used to efficiently resolve the boundary layer. Since the artificial dissipation is scaled isotropically with the spectral radii of the Jacobian matrices, the damping in the wall normal direction may become excessive. Ref. [25] proposed a 3D extension to the 2D variable scaling of Martinelli [26] which adjusts the levels of the blended 2<sup>nd</sup> and 4<sup>th</sup> order smoothing to be used in conjunction with the central difference convective fluxes. When the TVD convective discretization is chosen, this non-isotropic scaling affects only the waves which are subjected to the entropy cutoff [16],[2]. In such cases, the scaling takes a form similar to that found in Ref. [27].

## 3. Adaptation

Adaptation increases the accuracy of the discrete solution by locally reducing the local mesh dimension through directional division of mesh cells (physical cells). This process has evolved into a two-stage procedure. The detection/division stage begins by scanning a preliminary discrete solution for regions of interest. It then enhances the mesh in those regions through cell division to create new computational nodes. The second stage consists of mesh smoothing and surface reconstruction. This process controls both mesh stretching and cell skewing while maintaining an accurate representation of the surface geometry.

### 3.1 Detection/Division

The feature detection algorithm presently used is essentially a refinement of the technique used in the preliminary 2D investigations in Ref. [2]. This algorithm was extended to 3D viscous flow in Ref. [15] and is fully documented in Ref. [19]. The process consists of several steps which intend to isolate regions of locally high truncation error and then reduce this error through cell division. After first examining the domain with an undivided second difference of pressure to find "shock" cells, the routine re-scans only the remaining cells in the computation to locate "smooth" features. This second scan relies upon an undivided second difference of velocity magnitude to locate regions of rapidly varying shear stress and an undivided first difference of density to locate inviscid features in the flow. The cells tagged in the second scan are evaluated on a statistical basis as outlined in Ref. [23]. The division routine operates recursively in a

direction-by-direction manner and retains the ability to divide the cells directionally when features are nearly mesh aligned.

### 3.2 Mesh Smoothing

After the division process is complete, the entire mesh is smoothed through the sequential application of Laplacian and vector cross operators to reduce local stretching and skewing errors within the mesh. This step is important since the adaptation process will reduce the truncation error in the solution only if the mesh remains smooth as it refines.

Since they involve only first derivative terms, discrete solutions of purely inviscid flow problems are more tolerant of poor meshes. In 2D, for example, using trapezoidal integration to evaluate the inviscid flux integral in Eqs. {8} and {9} one may guarantee at least first-order accurate nodal updates (consistency) regardless of mesh quality[28]. Viscous simulations, however, require computing the first derivative of first derivatives - a process which compounds numerical errors due to mesh stretching or skewing. This fact makes it impossible to guarantee a consistent representation of the Navier-Stokes equations on an arbitrary mesh (assuming linear basis functions). These observations lead to the usual requirements of smoothly varying, non-skewed computational cells for accurate representation of viscous flows.

The elliptic smoothing process is separated into two relaxation operations. First, a Laplacian operator sweeps through the mesh nodes, relaxing a given node toward the mid-point location defined by the geometric center of its neighbors. This sweep proceeds on a direction-by-direction basis. The operator degenerates naturally on boundary faces or edges, so that such nodes remain free to slide along the face or edge.

After each pass with this smoother, the routine applies a vector cross operator to each physical cell in the mesh. For each mesh cell, this operator computes a right parallelepiped with the same median dimensions and uses a relaxation procedure to drive the corners of the physical cell

toward those of the right parallelepiped. In this manner, cell skewing is reduced throughout the mesh.

Although nodes are free to slide on and off boundary surfaces, neither smoother alters the mesh connectivity. After each smoothing pass, the algorithm checks to ensure that all cell volumes are physically meaningful. The smoother operates in about 10% of the time required for one solution iteration, and uses typical relaxation factors of approximately 0.1 with 10 steps.

### 3.3 Geometry Definition

Since the smoother allows mesh nodes to move along boundaries, surface nodes must be constrained to the body surface. This operation requires interrogation of a surface geometry data base. Such a data base also ensures that new points introduced on the surface through adaptation are placed directly upon that boundary.

Figure 5 presents a situation common to all adaptive schemes regardless of control volume shape. As shown in the figure, when a new point is introduced on a mesh boundary, it may not fall directly upon the body surface. The high aspect ratio cells typically found in Navier-Stokes simulations exacerbate this problem, and near a highly convex surface, several new nodes may be introduced which are actually inside the surface. To rectify this situation, all surface nodes are moved to the actual surface and a search algorithm then follows each computational coordinate (for as long as it exists) into the mesh to adjust interior nodes which may have been wrongly introduced inside the body.

Several approaches exist to relocate the surface points<sup>[29]</sup>. The present algorithm adopts an approach which requires only an unconnected surface point distribution on the body. This data base may be structured or unstructured and processing begins with a triangular tessellation of the surface data to form triangular patches describing the surface geometry. These patches are currently planar, although no fundamental difficulty exists in using a higher order description. Surface reconstruction begins by projecting a ray from each boundary node toward the surface

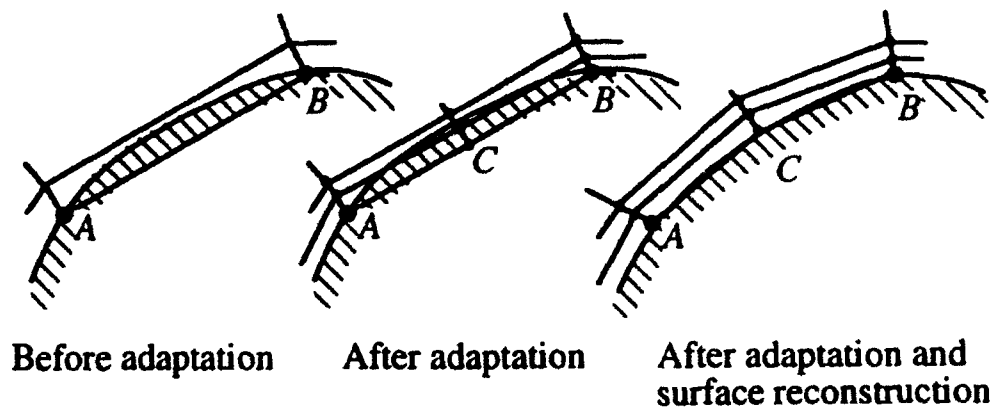


**Figure 5.** Reconstruction of surface geometry from surface database.

mesh. The algorithm then finds the triangle which is pierced by the projection ray and relocates the surface node to the point of intersection of the patch and the ray. Surface reconstruction is performed during alternating sweeps of the entire mesh smoother. Figure 6 demonstrates the process using a hemispherical surface, and an initially cubic arrangement of physical cells. The example shows results after only one iteration of the complete mesh smoothing algorithm. Successful experiments have mapped meshes onto a variety of convex and concave bodies including the examples in the next section and the 3D cropped delta wing in Refs. [15] and [19].



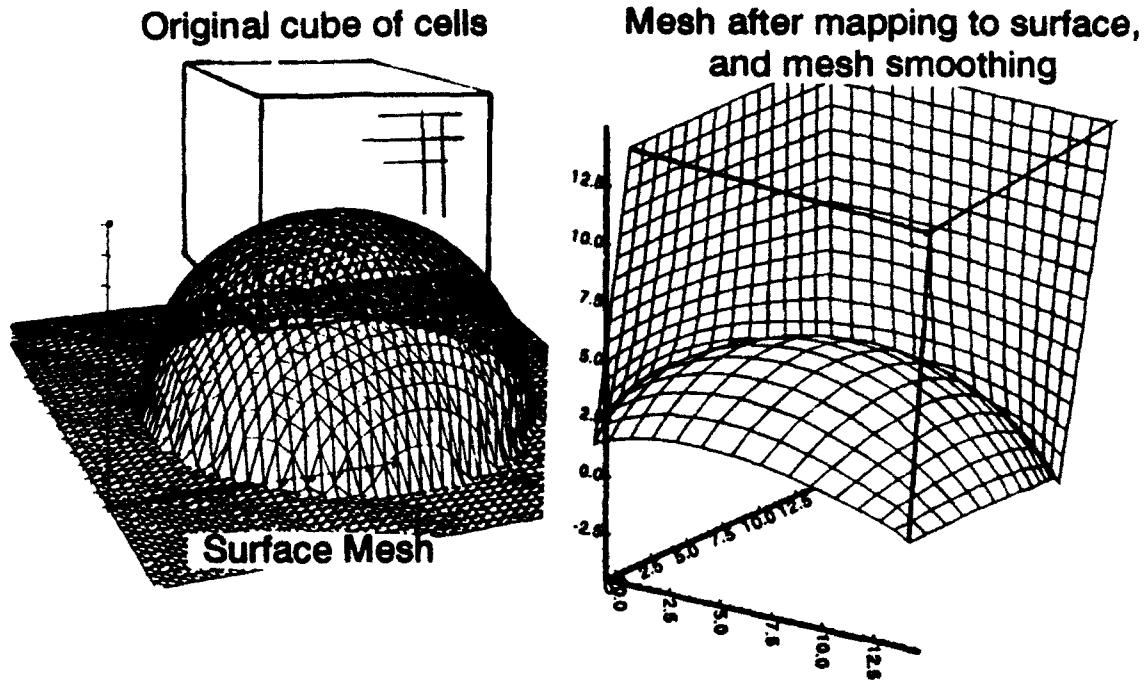


**Figure 6.** Triangulated surface geometry and resulting computational mesh after mapping physical cells onto surface. Original mesh consisted of  $14 \times 14$  cube. 1 smoothing pass, and 1 surface reconstruction sweep.

## 4. Numerical Experiments and Discussion

The numerical results contained within this section intend to focus the discussion on issues raised in the introduction and to provide an account of the scheme's behavior. Herein, attention is restricted to two-dimensional example problems. Refs. [15] and [19] present three dimensional results with the current method including comparison with experiment.

### 4.1 AGARD 03 Test Case

Before examining the behavior of the full viscous scheme, it is appropriate to establish the accuracy of the convective discretization and adaptive methodology. The AGARD 03 test case has been explored in the literature with a variety of methods<sup>[12],[30],[31]</sup>. It examines symmetric, inviscid, flow at Mach 0.95 over a NACA 0012 profile and the case presents a particular challenge to numerical schemes<sup>[12]</sup> since it contains strong coupling between smooth and discontinuous features which span many length scales. The flow becomes supersonic over the airfoil and forms an oblique "fish-tail" shock system attached to the trailing edge. A weak normal shock forms downstream of these shocks, in the wake of the airfoil. The smooth expansion over the airfoil surface weakens and bends the oblique shocks away from the body. Finally a shock triple point forms which locates the normal shock in the wake.

The shock polar at the  $7.99^\circ$  trailing edge of the airfoil is extremely steep at these Mach numbers and small changes in the trailing edge Mach number may radically alter the fish-tail shock

structure<sup>[12]</sup>. This sensitivity is further compounded by the fact that the shock triple point lies approximately 5 chords away from the airfoil. Stiffness in the crossflow direction makes this case quite sensitive to far field boundary placement. Successful prior calculations located the boundary about 100 chords away<sup>[12],[31]</sup>. Furthermore, fine resolution of the shocks in the wake does not ensure low overall truncation error since small errors in smooth regions of the flow may cause gross errors in shock location, regardless of resolution<sup>[12]</sup>. For these reasons, the problem directly addresses the issues of mesh convergence and consistency, raised earlier, while simultaneously evaluating the inviscid discretization.

The Mach contours in Figure 7 provide an overview of the discrete solution. In this simulation the entropy cutoff in the TVD scheme was applied to all eigenvalues. The figure shows both Mach contours and the final adapted half-mesh with 5 levels of mesh cells and approximately 18,000 nodes. The far field boundary in the calculation was located 75 chords away, and used the characteristic based treatment of Ref. [32]. Figure 8 shows an enlargement of the Mach contours in the region near the airfoil.

Mesh refinement studies in Ref. [12] using CFL2D and the floating shock fitting procedure of Ref. [31] provide a basis for evaluating the discrete solution. The finest mesh in these studies consisted of 1,567,485 nodes (2049 x 765) and the results from these studies located the normal shock (measured to the sonic line) between  $3.32c$  and  $3.35c$  downstream of the trailing edge. The current results place this structure at  $3.34 \pm 0.02c$ . The Mach number of the flow through the oblique shocks varied from 1.45 near the surface to 1.25 near the shock triple point. These values also match those from CFL2D.

## 4.2 Flat Plate Boundary Layer Flow

The viscous test cases begin with a simulation of flow over a flat plate at Mach 0.5 and Reynolds number of 5,000 per unit length. The case was run on unadapted meshes extending  $2.5L$  above and in front of the plate. Ref. [19] considers a similar example using the current method.

Entropy cutoff applied to all eigenvalues

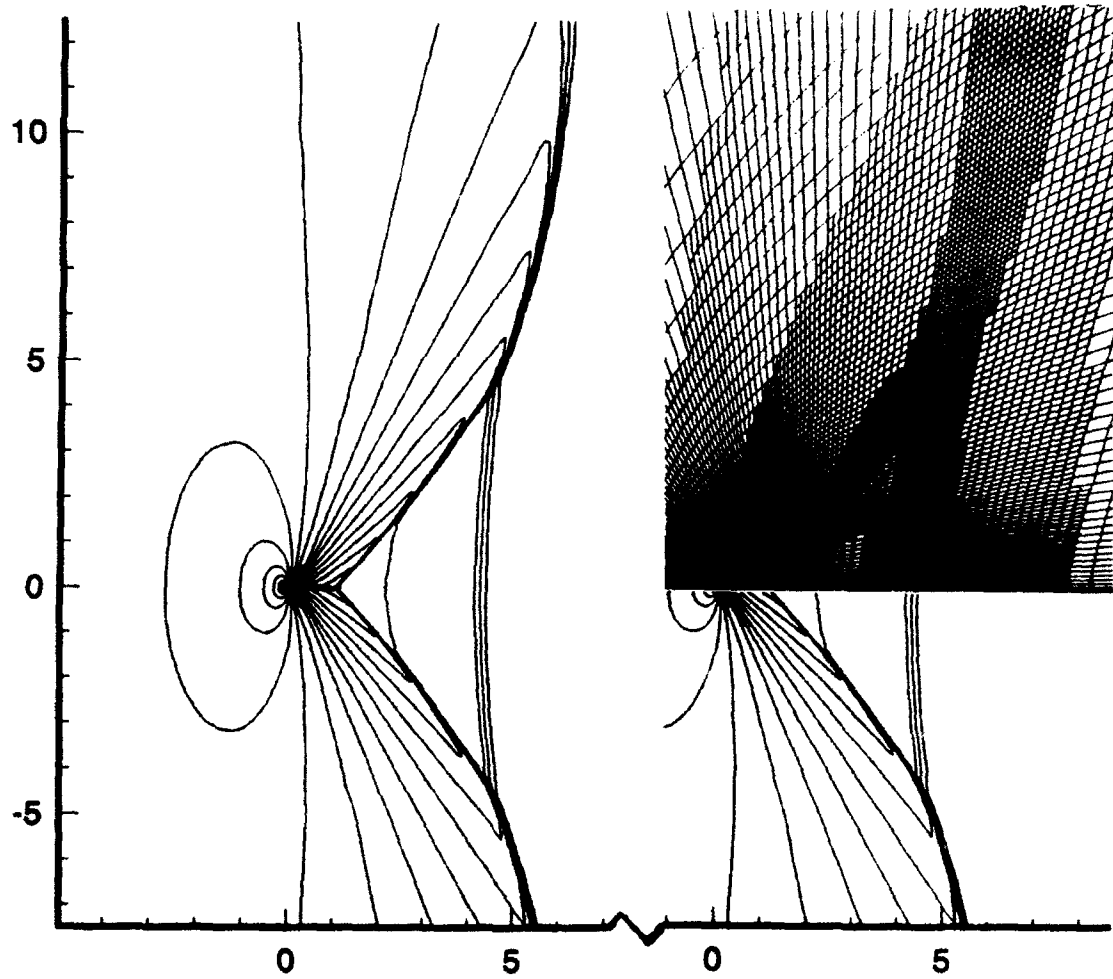


Figure 7. Mach contours (inc.=0.05) and adapted upper half mesh for AGARD 03 test case. Mach 0.95,  $\alpha = 0^\circ$ , inviscid flow. 18,000 nodes.

Entropy cutoff applied to all eigenvalues

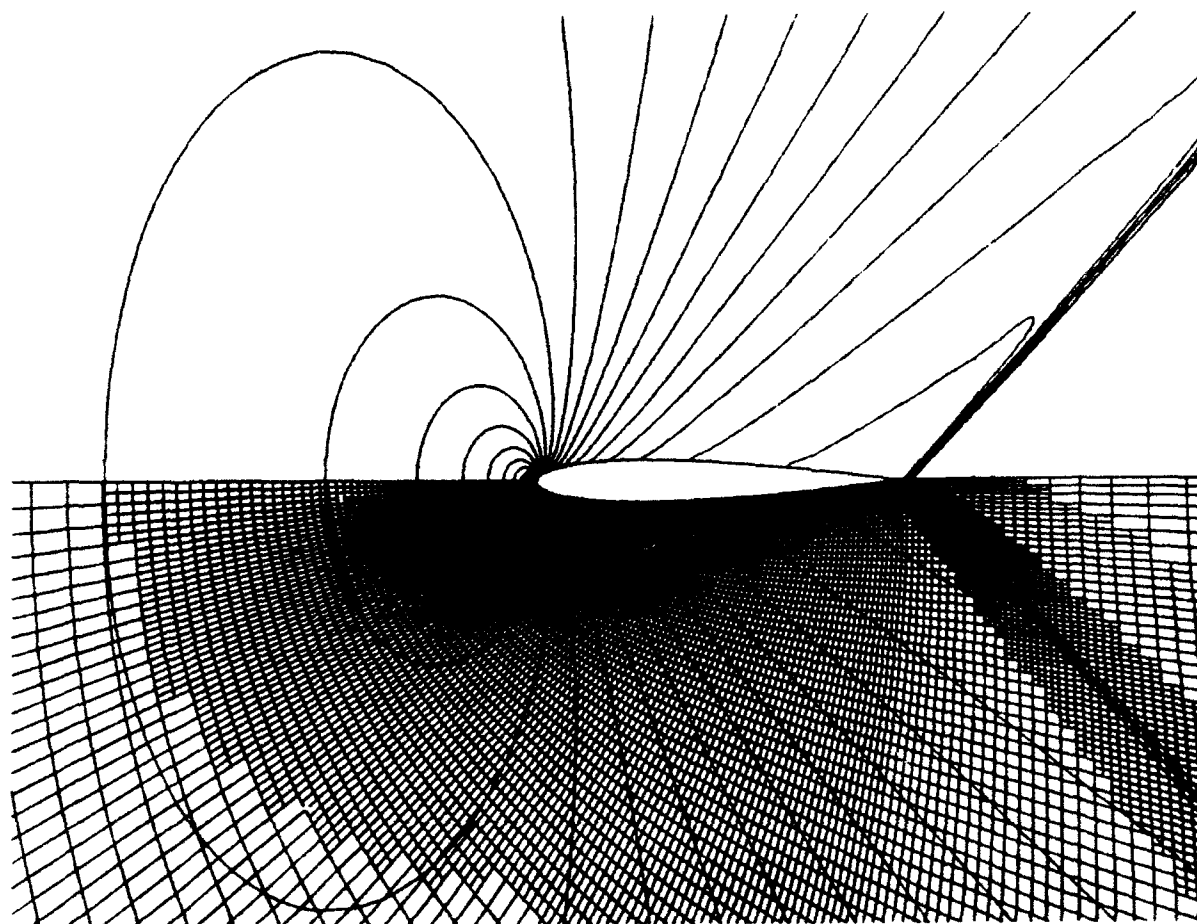


Figure 8. Near field Mach contours (inc.=0.05) for AGARD 03 test case.

However, the present discussions warrant reexamination of this case to provide insight into the scheme's behavior when the entropy cutoff is applied to all the eigenvalues.

The Upwind TVD convective formulation makes use of an entropy cutoff which precludes violation of the entropy condition at points where the eigenvalues vanish in the flow<sup>[17],[2],[19]</sup>. Since all linear eigenvalues become zero at solid walls, this cutoff may adversely affect the scheme's accuracy in such regions. Perhaps the most common approach to avoiding this situation is to apply the cutoff only to the nonlinear eigenvalues. Figure 9 presents  $u$ -velocity profiles plotted versus similarity parameter and compared directly with a Blasius profile. Two cases are examined, one in which all the eigenvalues were thresholded, and a second one which applied the cutoff only to the nonlinear waves. Since these effects are most obvious with relatively sparse boundary layer resolution, this example uses only about six points in the layer. Despite this apparent lack of resolution, when the cutoff,  $\delta$ , applied only to the nonlinear waves, the solution already provides a reasonable approximation of the Blasius profile. These results are typical of those obtained with high-resolution upwind methods and often lead to the practice of cutting off only the nonlinear waves in viscous flow simulations<sup>[33],[34]</sup>.

Previous results with the present scheme<sup>[15],[19]</sup> follow this approach and apply  $\delta$  only to the nonlinear waves. Figure 10, however, presents  $u$  and  $v$ -profiles obtained cutting all the waves in the solution, and using cutoff values of  $\delta = 0.01, 0.1, \text{ and } 0.3$ . By increasing the boundary layer resolution to about 13 points, the detrimental affects of  $\delta$  on the streamwise velocity nearly vanishes. For comparison, Figure 11 contains the same  $u$  and  $v$ -velocity profiles computed with the central difference option and 4th difference artificial dissipation ( $\nu_2 = 0.0, \nu_4 = 1/128 - 1/32$ ).

With 13 points in the boundary layer, agreement with the Blasius profile is excellent with both the central and TVD discretization of the inviscid terms. However, close examination reveals some slight discrepancies. These appear predominantly in the central difference results at  $\nu_4 = 1/32$  and  $1/64$ . Both of these curves display some evidence of a "viscous overshoot" just outside

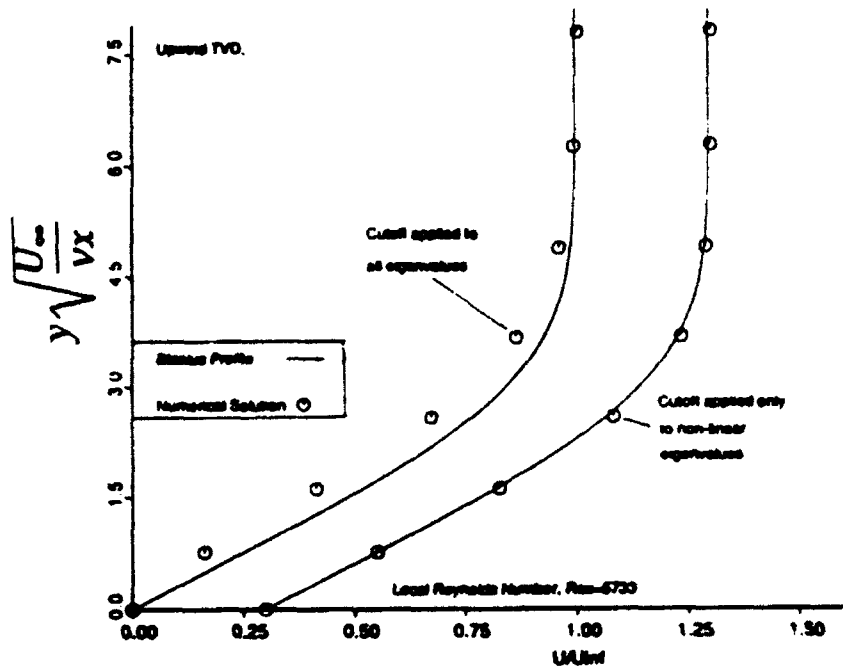
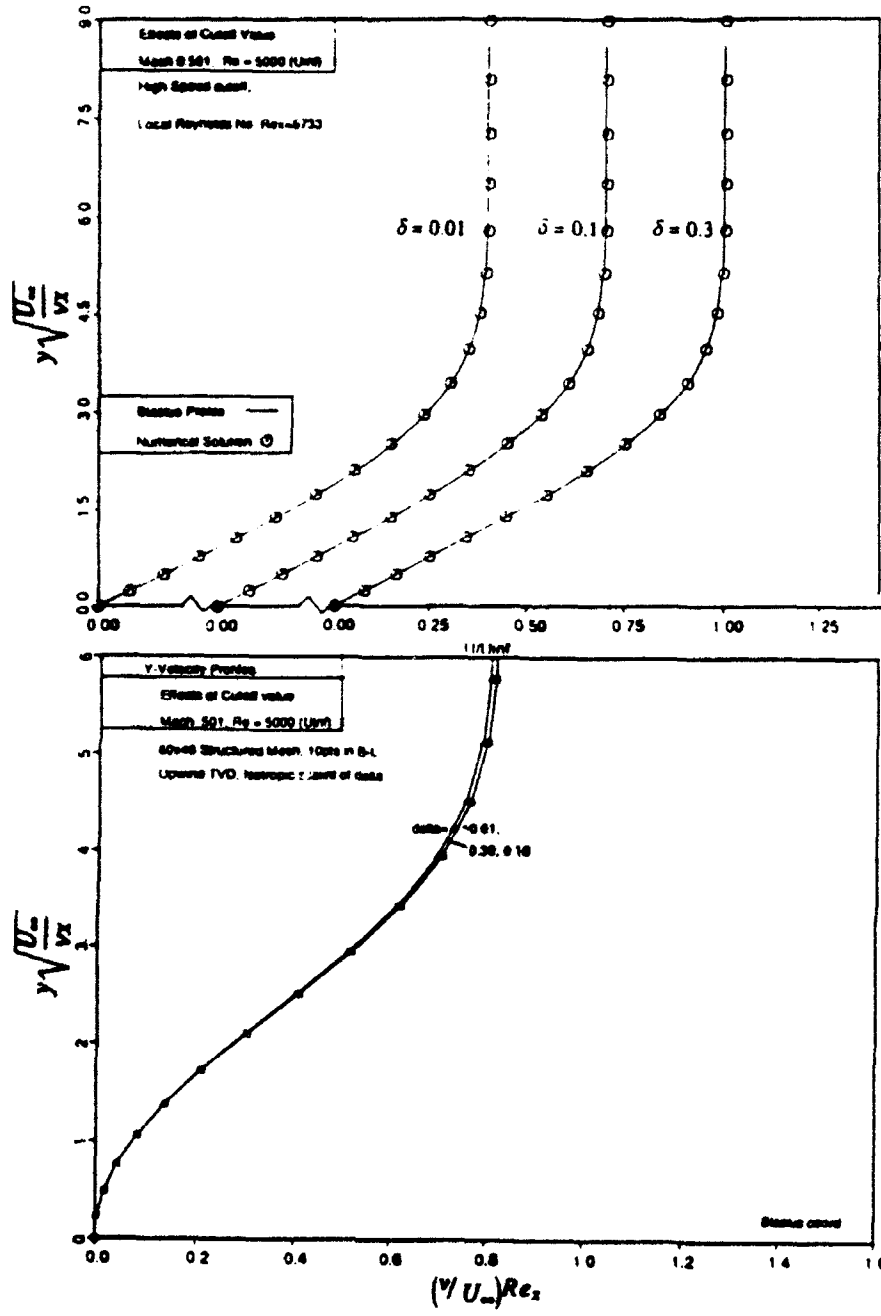


Figure 9. Effects of cutting off all or only the nonlinear eigenvalues on flat plate boundary layer simulation using the TVD discretization. Comparison with Blasius similarity solution,  $M_\infty = 0.5$ ,  $Re_L = 5,000$ .



**Figure 10.** Velocity profiles for flat plate boundary layer solutions using TVD convective discretization and applying the entropy cutoff to all eigenvalues. Above:  $u$ -velocity profiles. Below:  $v$ -velocity profiles, using 3 different values for the cutoff  $\delta$ .



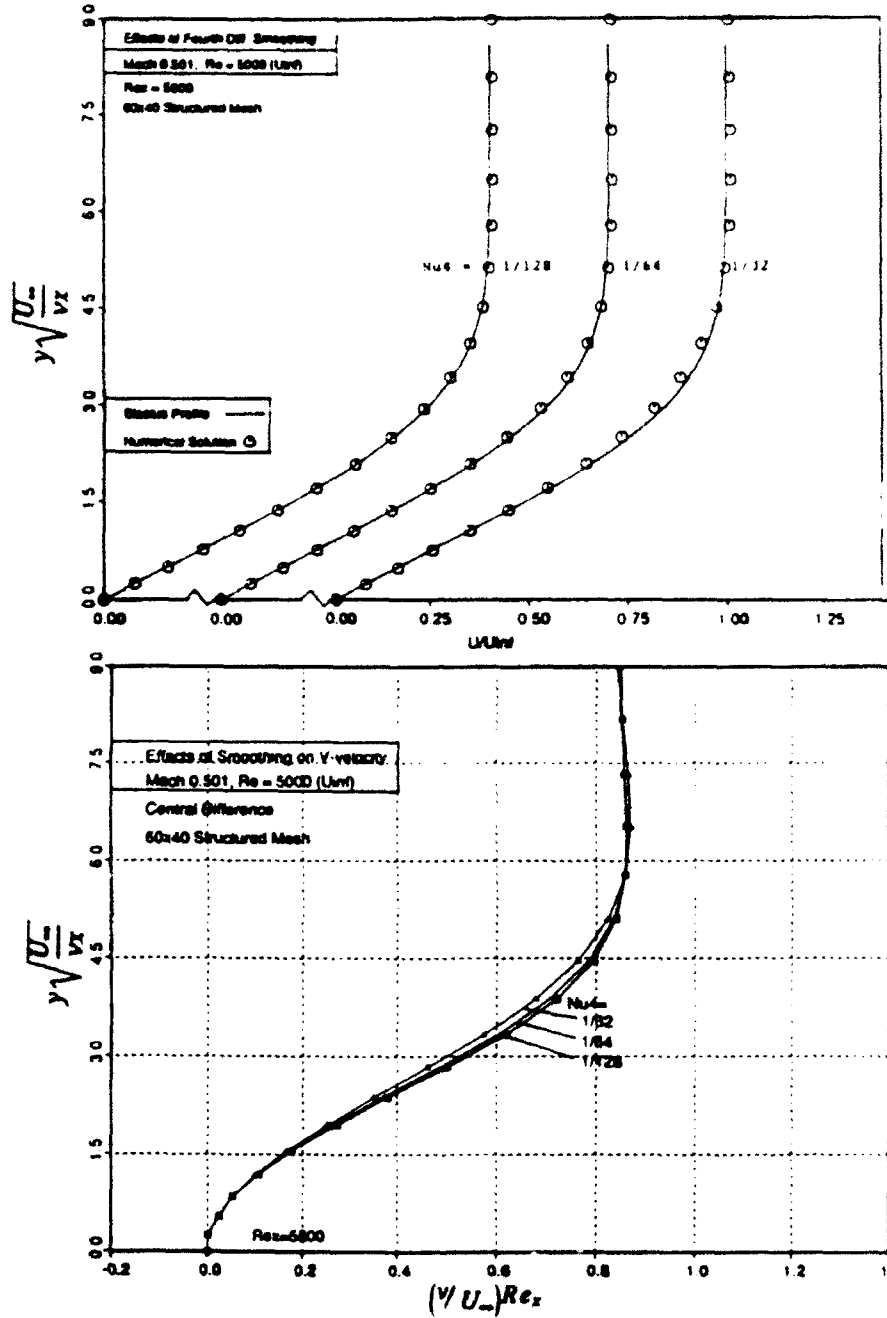


Figure 11. Velocity profiles for flat plate boundary layer solutions using central difference convective discretization with 4th difference artificial dissipation ( $\nu_4$ ). Above:  $u$ -velocity profiles. Below:  $v$ -velocity profiles, using  $\nu_4 = 1/32$ ,  $\nu_4 = 1/64$ , and  $\nu_4 = 1/128$ .

the knee of the profile. The excessive dissipation in these simulations does not permit the profile to bend rapidly enough to follow the Blasius profile around this knee. This error decreases rapidly with decreasing  $\nu_4$ , and almost no evidence of it is present in the simulation at  $\nu_4 = 1/128$ . The  $u$ -velocity profiles of the TVD discretization show almost no variation with the value of the cutoff,  $\delta$ . Additionally there is no evidence of the viscous overshoot, simply because the flux limiter would see such an overshoot as a "local maximum" and clip it off.

Slightly more variation is seen between the solutions in  $v$ - velocity profiles in Figs. 10 and 11. Here the viscous overshoot in the central schemes is much more readily apparent. Although the effects of the entropy cutoff are somewhat more apparent in these curves, the profiles for the TVD still remain quite similar to one another .

Figure 12 shows skin friction development along the flat plate. This plot reports results for both the central and TVD discretizations at two levels of resolution and compares these with the Blasius relation  $C_f' = 0.664(Re_x)^{-1/2}$ . With 13 points in the boundary layer (at a local  $Re_x$  of 5000), the theoretical skin friction is predicted well by about  $Re_x = 100$ , or 2% of the plate length from the leading edge. With 26 points in the layer, the skin friction matches almost immediately. With all the eigenvalues cutoff, lower resolution yields generally poor agreement between the TVD and Blasius result.

### 4.3 Symmetric Laminar Airfoil Test Case

The final example considers symmetric viscous flow over a NACA 0012 at a Mach number of 0.5 and Reynolds number of 5,000 with adiabatic wall boundary conditions. The recent literature includes investigations of this flow by a host of structured and unstructured methods<sup>[35],[36]</sup> and the case is well understood. In addition to these computational results, the relative simplicity of the flow permits an analytic analysis which provides an independent check of self-consistency in the discrete solutions.

As it is given in Ref. [37], the airfoil profile does not quite close at the trailing edge. This shortcoming was circumvented by continuing the profile until reaching the centerline and then rescaling both axes to place the trailing edge again at 1.0. Such detail is important in this flow since the case is near the upper boundary for stable laminar flow. Additionally, at the conditions of this simulation, a separation bubble appears at the trailing edge, and the separation location depends directly on the geometry of the trailing edge.

Figure 13 displays a view of the final adapted mesh in the vicinity of the airfoil. The starting mesh for this calculation was a 25x15 half C-mesh, and the final adapted mesh contained 5 levels of cells and 8,100 nodes. Two inset regions on this mesh show the finest two levels of adaptation near the leading and trailing edges.

One particular challenge presented by this test case lies in properly resolving the extent of the thin separation bubble at the trailing edge. In resolving this structure, the adaptation routine has changed the cell aspect ratio from approximately 20:1 to only 5:1 near the separation point. The final two adaptations divided cells primarily in the streamwise directions. As a result the cell aspect ratio on the wall varies from about 50 at the midchord to only 5 near the separation location. It is interesting to note that in the nonadaptive efforts in Refs. [35] and [36] the cells had approximately the same streamwise spacing, but used between 1/2 and 1/5 the wall normal mesh spacing. The current procedure arrived at this streamwise spacing by adaptation without user intervention.

Figure 14 presents contours of constant Mach number near the airfoil and an enlargement showing computed streamlines near the trailing edge. Figure 15 displays the variation in surface pressure and skin friction coefficients over the airfoil. These profiles agree well with established previously published results<sup>[35],[36]</sup>.

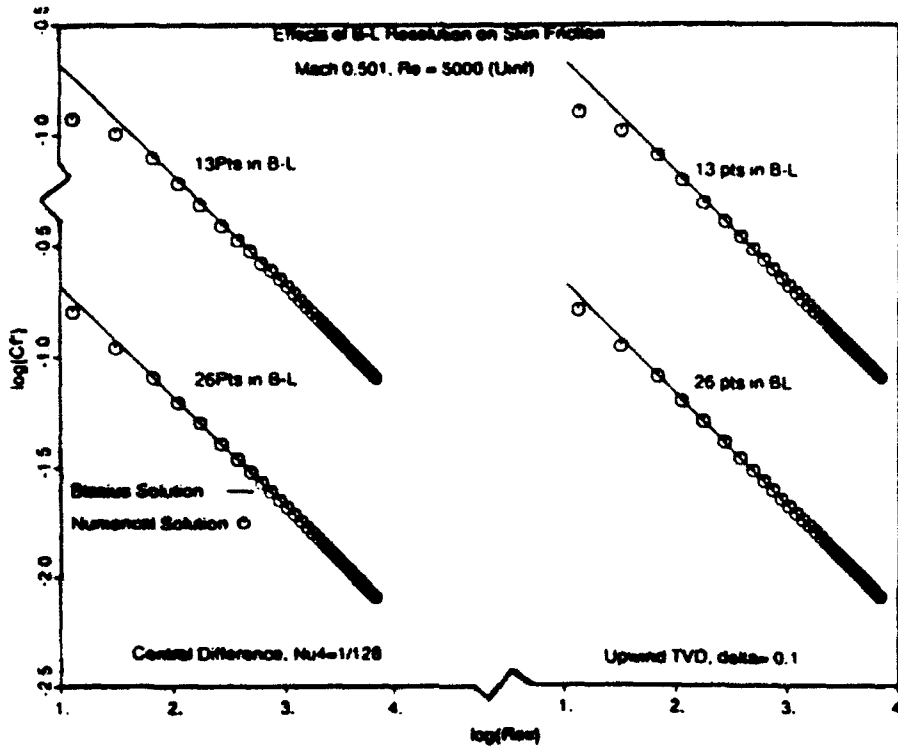


**Figure 12.** Skin friction evolution along flat plate using both Upwind TVD and central differencing. Entropy cutoff applied to all eigenvalues in TVD solutions. Blasius solution provided for comparison.  $M_\infty = 0.5$ ,  $Re_L = 5,000$ .

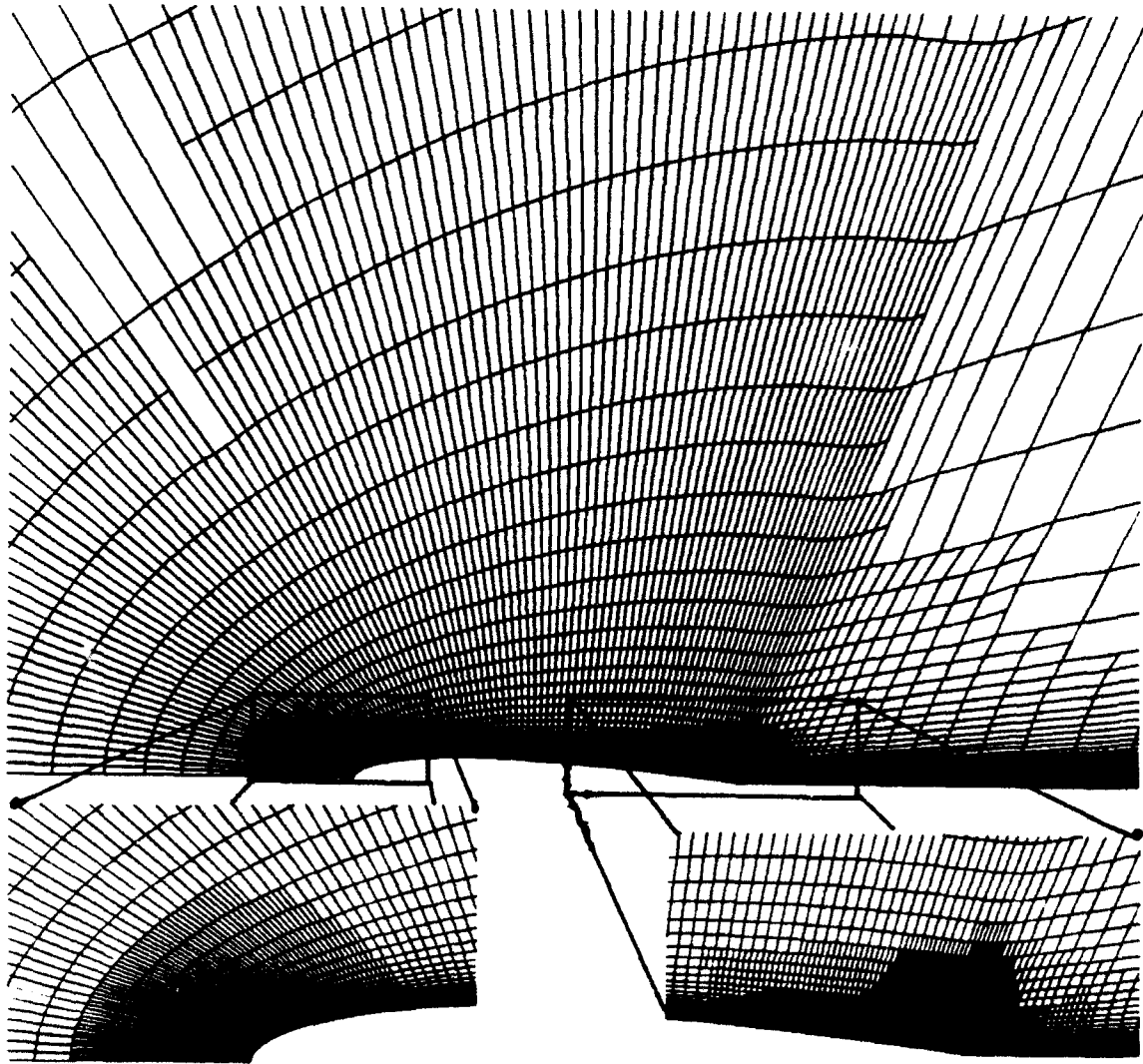


**Figure 13.** Adapted half-C mesh near airfoil for viscous NACA 0012 test case. 5 levels of cells, 8,100 nodes,  $M_\infty = 0.5$ ,  $Re_c = 5,000$ .

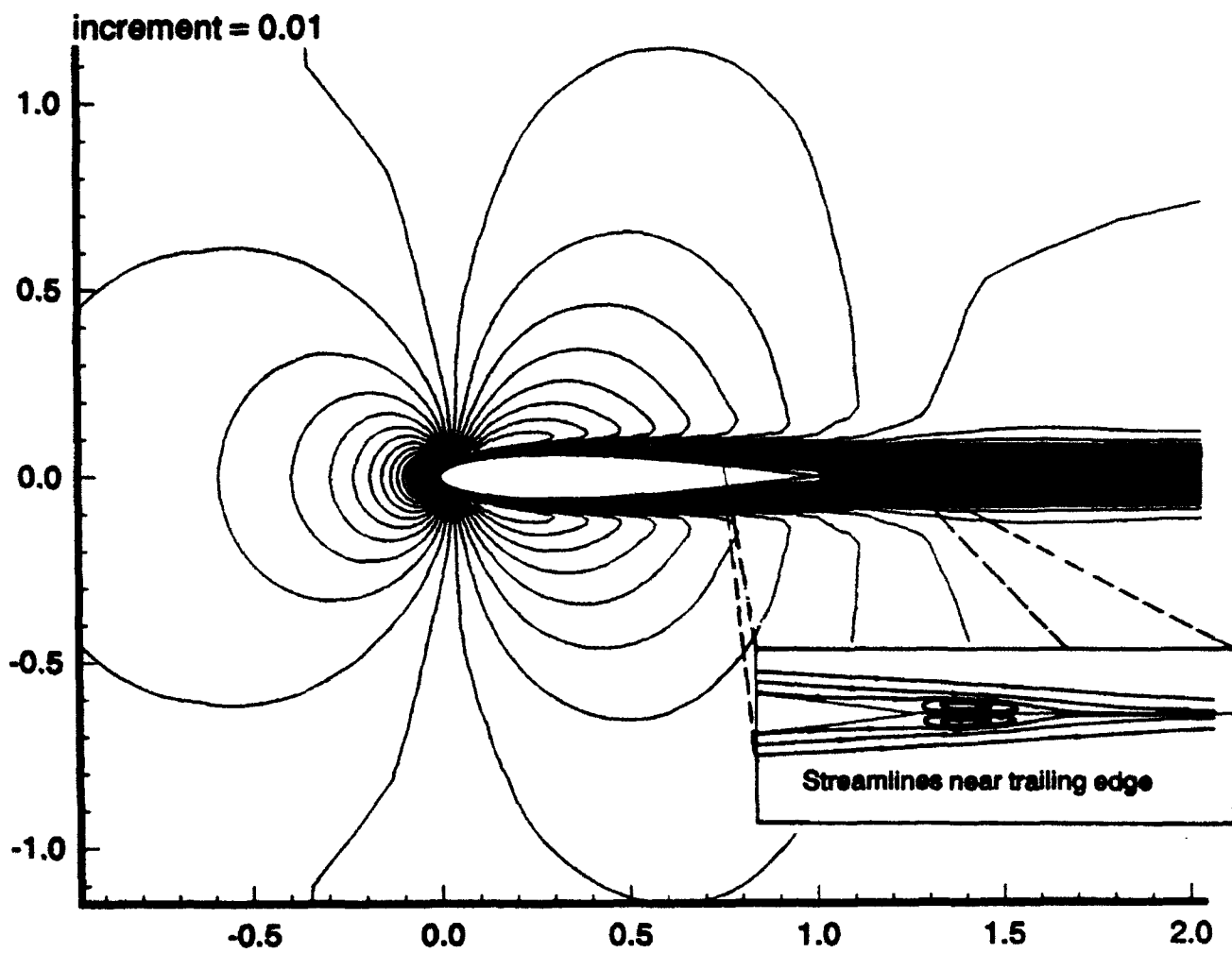


**Figure 14.** Mach contours (inc. = 0.01) in discrete solution using TVD discretization and applying entropy cutoff to all eigenvalues. Separation point at 81.5% chord.  $M_\infty = 0.5$ ,  $Re_c = 5,000$ .

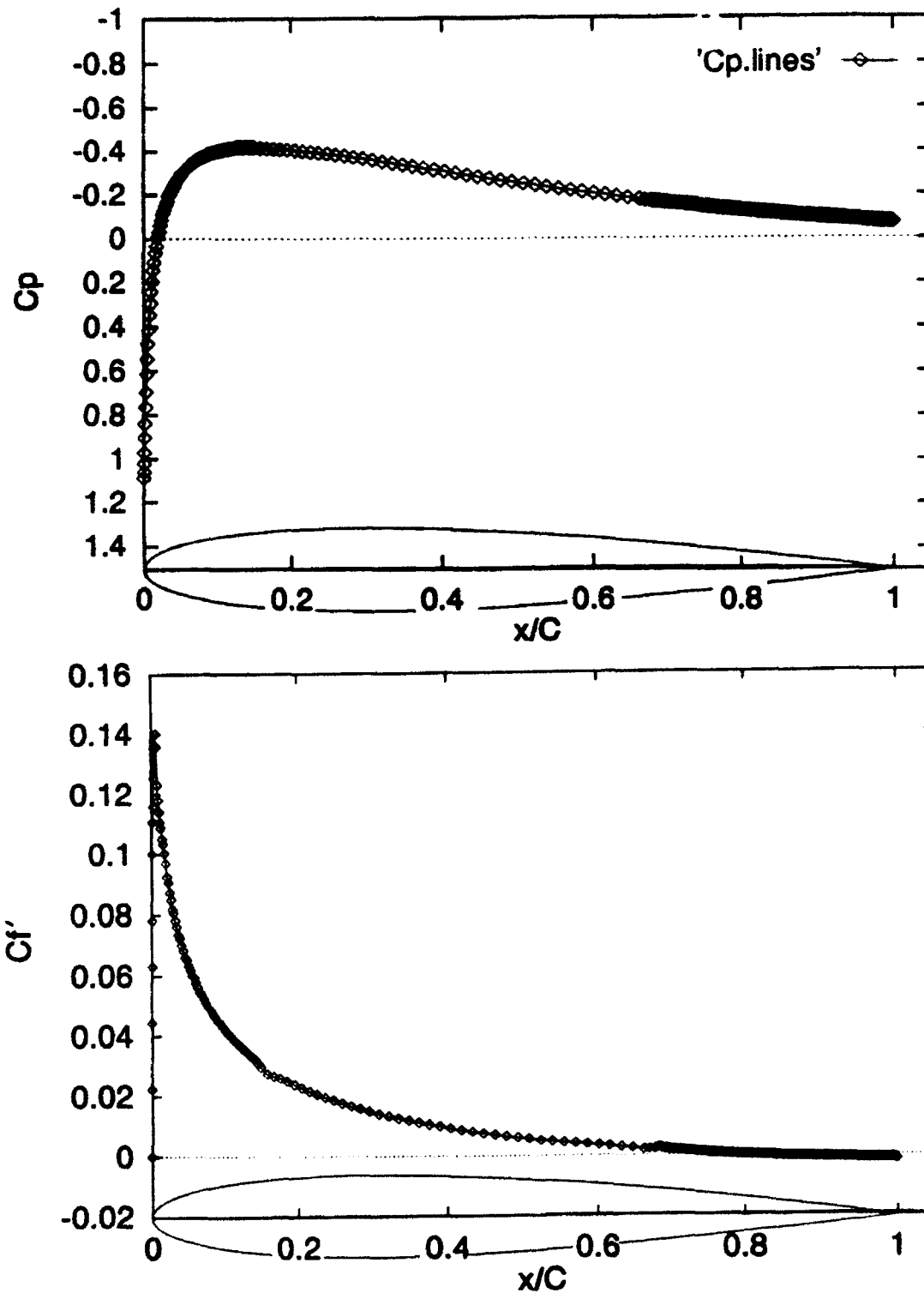


Figure 15.  $C_p$  and  $C_f$  profiles for NACA 0012 at  $M_\infty = 0.5$  and  $Re_c = 5,000$ . Entropy cutoff applied to all eigenvalues.

#### 4.4 Separation Location

Table 1 compares the location of the separation point as computed with several methods. Figure 16 shows streamlines and velocity vectors near the separation region, and has the half saddle of separation labeled on the surface. As indicated in the table, Ref. [35] showed that this location was sensitive to the level of numerical dissipation in the solution.

With the current method, dissipation enters from the entropy cutoff and from the discretization error. The adaptation present in the final solution aims to reduce this error by refining the mesh. Since the separation location is sensitive to the level of numerical dissipation, it is useful to examine its behavior as the mesh refines. Figure 17 traces the separation location on the last four meshes used in the solution process. As the background dissipation is reduced by mesh refinement, the separation point moves to a location consistent with a solution of the governing equations (since the modified PDE's approach the true governing equations). It is interesting to see the extent to which the last two adaptations affected the location of the separation point, since the cells were divided only in the streamwise directions and the wall normal mesh spacing remained constant.

Although the curve in Fig. 17 appears to flatten, it does not actually asymptote convincingly to the value of 81.5% reported earlier. Equation (18) provides a means to further investigate the magnitude of the discretization error in the immediate vicinity of the separation point.

$$\tan(\theta) = -3\mu \frac{\partial \omega}{\partial x} \bigg/ \frac{\partial p}{\partial x} \quad (18)$$

Table 1. Separation locations predicted by several methods.

Method	Dissipation	Sep. Loc. (%)	Wall spacing
Present Method	$\delta = 0.1$	81.5	0.001
Triangular scheme of [35]	$\nu_f = 1/256$	81.4	0.0002
Triangular scheme of [35]	$\nu_f = 1/64$	83.4	0.0002
Central Diff Method of [26]	N/A	81.9	N/A
Central Diff Method of [36]	N/A	81.1	0.0006



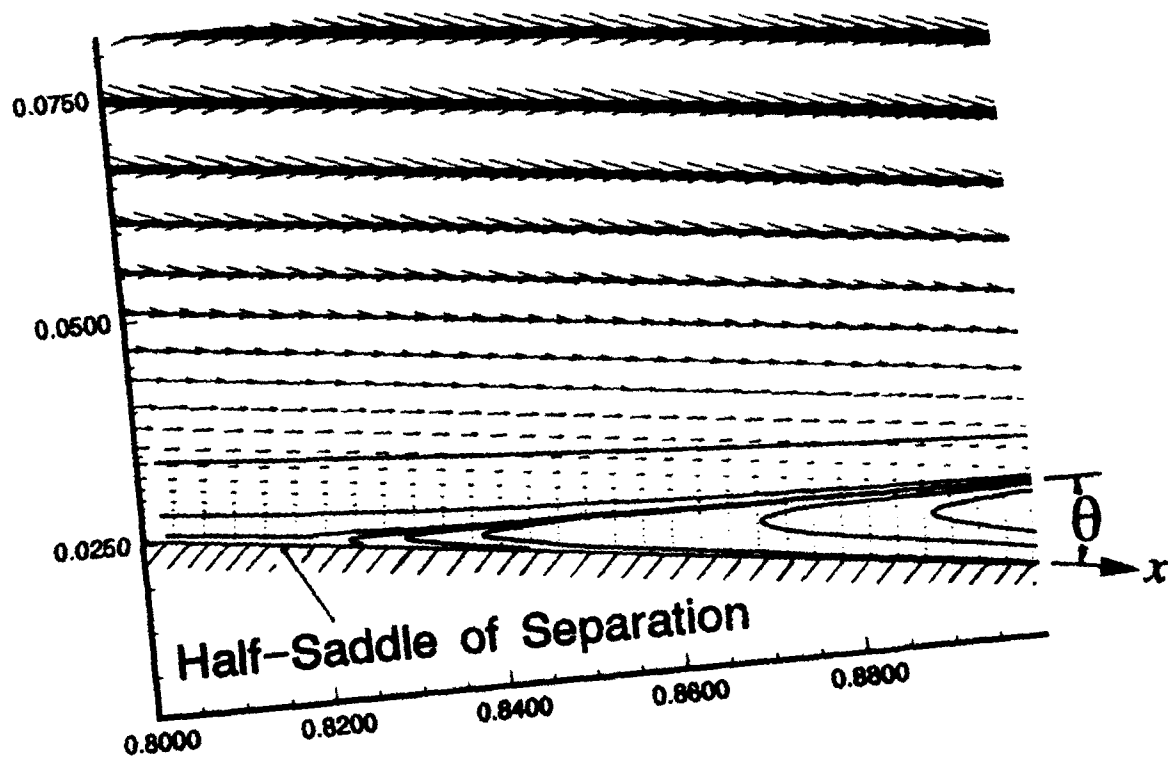


Figure 16. Velocity vectors and computed streamlines near separation point at trailing edge of airfoil.

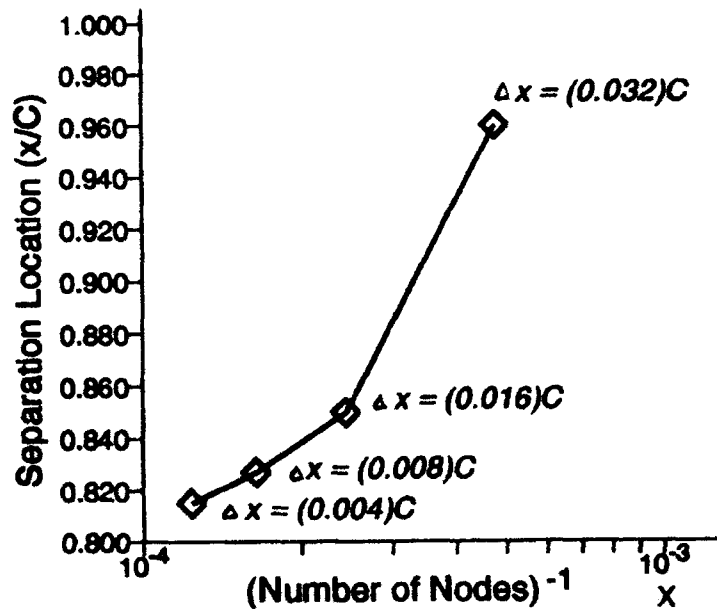


Figure 17. Variation of separation location with mesh refinement.  $\Delta x$  is the mesh spacing in the streamwise direction

This expression for the classical two-dimensional, laminar separation angle,  $\theta$ , was derived in Ref. [38]. In Ref. [39] the authors arrive at the same expression from critical point theory where they show that the slope of the isocline emanating from a half-saddle of separation may be derived from a direct balance between the normal and tangential momentum equations. This facilitates a direct comparison between the measured angle in Fig. 16 and the angle predicted by a local solution of the (incompressible) Navier-Stokes equations. The measured separation angle in Figure 16 is  $6.07 \pm 0.2^\circ$ , while evaluating Eq. (18) numerically results in  $\theta = 6.09 \pm 0.14^\circ$ .

This analysis does not verify the location of the separation point, but it does indicate that the discretization error in the region of the separation is very small. Thus, the extent of the separation bubble is not "held back" by locally high, nonphysical, dissipation or other discretization error. For comparison, performing the same analysis on the coarsest mesh in Fig. 17 (sep. location. at 96%) yields a  $9.5^\circ$  discrepancy between the measured and computed isocline angles, indicating large discretization errors.

#### 4.5 Entropy Cutoff and Non-Physical Solutions

The preliminary computation of this viscous NACA 0012 test case adopted the usual approach of applying the entropy cutoff to only the nonlinear waves in viscous simulations. While converging after the second adaptation (3rd mesh), the method resulted in solutions similar to that shown at the right of Figure 18. Such nonphysical solutions persisted for CFL numbers from 0.1 to 4.3 and for 3 and 5 stage Runge-Kutta schemes, using local or global time steps. The problems were considered anomalous since the same code has performed well in a variety of two- and three-dimensional test cases<sup>[15],[19]</sup>. The problem was solved by applying the entropy cutoff to all wave speeds, and it is this experience which motivated the inclusion of the flat plate investigation with all the eigenvalues cut.

The appearance of such behavior in an otherwise well behaved and well-documented solver warrants some discussion. Similar anomalous results have been documented by several authors [33],[34],[40],[41]. Ruling out bugs in the code (based upon previous success with a wide variety

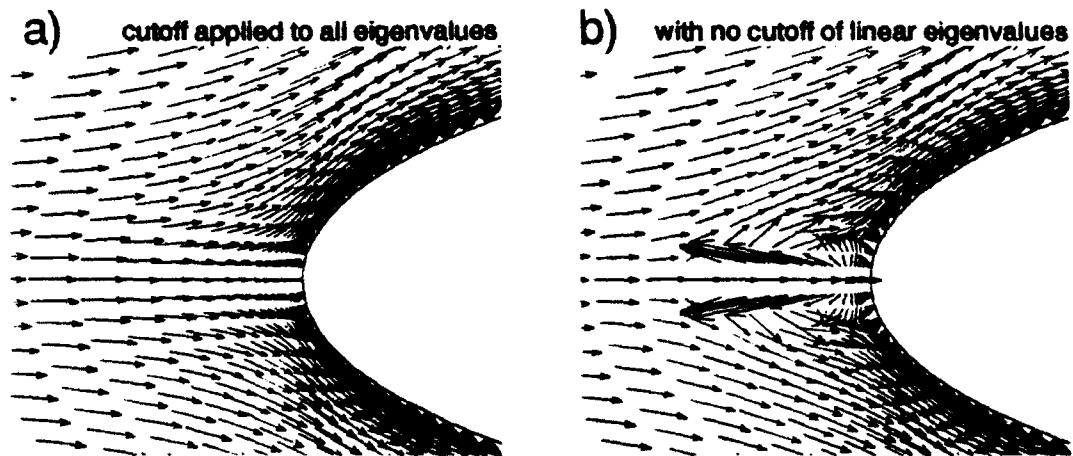


**Figure 18.** Stagnation region at leading edge of NACA 0012 after second adaptation. Frame a: entropy cutoff of  $\delta = 0.1$  applied to all eigenvalues. Frame b: entropy cutoff of  $\delta = 0.1$  applied to nonlinear eigenvalues only.

of test cases), the two most likely explanations are: 1) problems in the TVD scheme itself, 2) problems resulting from the interaction of the TVD-inviscid and central-viscous discretizations.

Close examination of Fig. 18b shows that the boundary layer near the stagnation point remains well behaved. It is only in the inviscid stagnation region outside this viscous layer that problems arise. In that region, the viscous terms are smaller by 2-3 orders of magnitude than near the "knee" of the boundary layer profile. This statement favors explanation #1, and shifts focus to the TVD scheme itself. The only difference in the inviscid discretization used in Fig. 18b and a standard inviscid flow (like the AGARD 03 test case) is the fact that, in 18b, the linear eigenvalues in the viscous flow were not thresholded near zero.

The cutoff,  $\delta$ , is introduced into the method to prevent violation of the entropy condition<sup>[16]</sup>. When the cutoff is invoked, it introduces (2nd difference like) explicitly added dissipation. The added dissipation term increases the entropy, and only physically consistent results should remain in the space of possible discrete solutions. In the stagnation region, all the linear eigenvalues go to zero. In the inviscid part of this stagnation region, if no dissipation is introduced, the preference for selecting a solution consistent with the entropy condition is lost. On a coarse enough mesh, the dissipation introduced through the discretization error may be sufficient to rule out such inconsistent discrete solutions. However, when the mesh is refined (as by adaptation), such dissipation will diminish at a rate determined by the order of accuracy of the scheme. Therefore, on a fine enough mesh, nonphysical solutions may appear. Such a hypothesis explains the converged and physically consistent results obtained on the first two meshes in the adaptation sequence. Notice that inside the boundary layer,  $u$  also tends to zero. Here, however, the viscous terms in the Navier-Stokes equations generate entropy with the apparent result of "selecting" physical solutions. This statement is supported by the seemingly well behaved velocity vectors seen just inside the boundary layer in Fig. 18b.

Further supporting evidence for this hypothesis came from examining the region near the saddle point of separation. Near the point of inflection in the velocity profile, the virtual lack of

curvature gives rise to generally small viscous stresses. When this point is near the wall, the velocities are also small and so the eigenvalues will tend to vanish and discretization may violate the entropy condition. Investigation of the flow topology in this area revealed physically inconsistent streamline patterns in the vicinity of the separation point just away from the wall. These arguments are not intended as proof, but do offer avenues for further investigation.

This problem in inviscid stagnation regions reemphasizes the need for thresholding of the wave speeds in schemes which may violate the entropy condition. In complex flows, errors such as the inconsistent flow topology cited here could easily go unnoticed and give rise to unpredictable flow physics. This statement goes against the common practice of thresholding only some of the waves, or different waves in different directions in the domain<sup>[33],[40],[19]</sup>. While such techniques may produce excellent results for skin friction and heat transfer they still do not, in general, ensure convergence to only physically consistent solutions.

## 5. Summary and Conclusions

This work presented further details of a newly developed unstructured discretization for modeling the viscous terms in the Navier-Stokes equations. A detailed description of this discretization and its implementation was presented in a form requiring only cell-to-node and node-to-cell communication. The method yields second-order accuracy on smooth meshes, and is free stream preserving on any arbitrary mesh. Various aspects of the technique were evaluated through test problems, analysis and mathematical proof. The method was incorporated into a previously documented adaptive TVD scheme using hexahedral based unstructured meshes which adapt to the evolving solution through directional cell division. The discussion also outlined the techniques developed for controlling mesh quality and reconstructing the correct surface geometry after adaptation and mesh smoothing.

The issue of mesh convergence was investigated through examination of the AGARD 03 test case which is known to be particularly challenging to adaptive schemes. The new scheme matched results from previously reported mesh convergence studies conducted with two structured schemes. These discrete solutions also agreed with the results of two adaptive upwind schemes which used a feature detection algorithm specifically designed in response to the subtlety of the AGARD 03 test case.

A detailed examination of viscous flow over a NACA 0012 at  $M_\infty=0.5$  and  $Re_c = 5,000$  resulted in  $C_p$  and  $C_f$  distributions which agreed well with previously published solutions on unadapted

meshes. In addition, the separation location was predicted in agreement with previous findings and further supported by an analysis of the theoretical laminar separation angle.

During the course of the investigations, it became evident that the common practice of thresholding only the nonlinear eigenvalues when using upwind methods whose formulation permits violations of the entropy condition can admit nonphysical discrete solutions. Such violations are likely in stagnation regions and near points of inflection in the boundary layer velocity profile. Such solutions were examined and related to similar anomalous solutions reported by a variety of other researchers also using Roe type schemes. Since many of these nonphysical solutions may go undetected in complex flow, this research advocates the (admittedly conservative) position of always thresholding both the linear and nonlinear eigenvalues in all directions. While this approach does slightly increase the resolution requirements for accurate representation of the boundary layer, it appears to be the only sure way to avoid admitting nonphysical solutions into the solution space. A detailed evaluation of discrete solutions to a flat plate boundary layer was included showing good skin friction prediction with approximately 13 points despite thresholding all of the eigenvalues.



## 6. References

- [1] Barth, T.J., Jespersion, D.C. "The Design and Application of Upwind Schemes on Unstructured Meshes," *AIAA Paper - 89-0366*, 1989.
- [2] Aftosmis, M., and Kroll, N., "A Quadrilateral Based Second-Order TVD Method for Unstructured Adaptive Meshes," *AIAA 91-0124*, 1991.
- [3] Rumsey, C.L., *Development of a Grid Independent Approximate Riemann Solver*, Ph.D. Dissertation, Univ. of Michigan, 1991.
- [4] Roe, P.L., and Beard, L., "An Improved Wave Model for Multidimensional Upwinding of the Euler Equations," *Proceedings of the 13<sup>th</sup> International Conference on Numerical Methods in Fluid Mechanics*, Rome, Italy, 1992.
- [5] Catalano, L.A., De Palma, and P., Pascasio, G., "A Multi-Dimensional Solution Adaptive Multigrid Solver for the Euler Equations," *Proceedings of the 13<sup>th</sup> International Conference on Numerical Methods in Fluid Mechanics*, Rome, Italy, 1992.
- [6] Dannenhoffer, J.F. III., *Grid Adaptation for Complex Two-Dimensional Transonic Flows*. Sc.D. Thesis, Massachusetts Institute of Technology, Cambridge MA, 1987.
- [7] Mavriplis, D.J., *Solution of the Two-Dimensional Euler Equations on Unstructured Triangular Meshes*, Ph.D. Dissertation, Princeton Univ., 1987.
- [8] Löhner, Morgan, K., and Zienkiewicz, O.C., "The Solution of Nonlinear Systems of Hyperbolic Equations by the Finite Element Method," *International Jol. of Numerical Methods in Fluids 4*, pp.1043-1063, 1984.
- [9] Morgan K., Peraire, J., and Peiro J., "Unstructured Grid Methods for Complex Flows," *AGARD-R-787*, May 1992.

- [10] Löhner R, and Baum J., "Numerical Simulation of Shock Interaction with Complex Geometry Three Dimensional Structure Using a New Adaptive H-Refinement Scheme on Unstructured Grids." *AIAA-90-0700*, January 1990.
- [11] Frink, N.T., Parikh, P., and Pirzadeh, S., "A Fast Upwind Solver for the Euler Equations on Three-Dimensional Unstructured Meshes," *AIAA-91-0102*, January 1991.
- [12] Warren, G.P., Anderson, W.K, Thomas, J.L., and Krist, S.L., "Grid Convergence for Adaptive Methods," *AIAA-91-1592-CP*, 1991.
- [13] Baker, T.J., "Element Quality in Tetrahedral Meshes," 7th International Conference on Finite Element Methods in Flow Problems, April 1989.
- [14] Baker, T.J., "Developments and Trends in Three-Dimensional Mesh Generation," *Applied Numerical Mathematics* 5, pp.275-304, 1989.
- [15] Aftosmis, M., "A Second-Order TVD Method for the Solution of the 3D Euler and Navier-Stokes Equations on Adaptively Refined Meshes," *Proceedings of the 13<sup>th</sup> International Conference on Numerical Methods in Fluid Mechanics*, Rome, Italy, 1992.
- [16] Harten, A., "High Resolution Schemes for Hyperbolic Conservation Laws," *Journal of Computational Physics*, Vol. 43, pp. 357-393, 1983.
- [17] Yee, H.C., and Harten, A. "Implicit TVD Schemes for Hyperbolic Conservation Laws in Curvilinear Coordinates," *AIAA Journal*, Vol 25, pp. 266-274, 1987.
- [18] Roe, P.L., "Error Estimates for Cell-vertex Solutions of the Compressible Euler Equations," ICASE Report No. 87-6, 1987.
- [19] Aftosmis, M.J., "An Upwind Method for the Solution of the 3D Euler and Navier-Stokes Equations on Adaptively Refined Meshes," WL-TR-92-3107, October 1992.
- [20] Kroll, N. and Rossow, C. "A High Resolution Cell Vertex Scheme for the Solution of the Two and Three Dimensional Euler Equations," *12<sup>th</sup> International Conference on Numerical Methods in Fluid Dynamics*, Oxford, GB, 1990.
- [21] Kroll, N., Gaitonde, D., and Aftosmis, M., "A Systematic Comparative Study of Several High Resolution Schemes for Complex Problems in High Speed Flows," *AIAA Paper - 91-0636*, 1991.

- [22] Jameson, A., "A Vertex Based Multigrid Algorithm for Three Dimensional Compressible Flow Calculations," in *Numerical Methods for Compressible Flows - Finite Difference, Element, and Volume Techniques*, Ed. by T.E. Tezduar and T. Hughes, Applied Mechanics Div. 78, ASME, NY, 1986.
- [23] Kallinderis, Y. and Baron, J.R. "Adaptation Methods for a New Navier-Stokes Algorithm," *AIAA 87-1167*, 1987.
- [24] Barth, T.J., "Aspects of Unstructured Grids and Finite-Volume Solvers for the Euler and Navier-Stokes Equations," *AGARD-R-787*, May 1992.
- [25] Radespiel, R., Rossow, C., and Swanson, R. C., "Efficient Cell-Vertex Multigrid Scheme for the Three-Dimensional Navier-Stokes Equations," *AIAA Jol.*, Vol. 28, No. 8. pp. 1464-1472, 1990.
- [26] Martinelli, L., "Calculations of Viscous Flows with a Multigrid Method," *Ph.D. Thesis*, Dept. of Mechanical and Aerospace Engineering, Princeton Univ., 1987.
- [27] Müller, B., "Simple Improvements of an Upwind TVD Scheme for Hypersonic Flow," *AIAA-89-1977-CP*, 1989.
- [28] Roe, P.L., "Error Estimates for Cell-vertex Solutions of the Compressible Euler Equations," ICASE Report No. 87-6, 1987.
- [29] Baker, T.J., "Shape Reconstruction and Volume Meshing for Complex Solids," *International Jol for Numerical Methods in Engineering*, Vol. 32. pp.665-675, 1991.
- [30] Hartwich, P., "A Fresh Look at Floating Shock Fitting," *AIAA 90-0108*, January 1990.
- [31] Warren, G.P., "Adaptive Grid Embedding for the Two-Dimensional Euler Equations," *AIAA 90-3049-CP*, 1990.
- [32] Whitfield, D.L., "Three-Dimensional Unsteady Euler Equation Solutions Using Flux Vector Splitting," *Short Course on Numerical Grid Generation*, Mississippi State University, June 1989.
- [33] Gaitonde, D.G., and Shang, J.S., "The Performance of Flux-Split Algorithms in High-Speed Viscous Flow," *AIAA 92-0186*, January 1992.

- [34] Riedelbauch, R., and Brenner, G., "Numerical Simulation of Laminar Hypersonic Flow Past Blunt Bodies Including High Temperature Effects," *AIAA 90-1492*, June 1990.
- [35] Mavriplis, D., J., "Multigrid Solution of the Navier-Stokes Equations on Triangular Meshes," *AIAA Jol.* Vol.28, No. 8, 1990.
- [36] Swanson, R.C., and Turkel, E., "Artificial Dissipation and Central Difference Schemes for the Euler and Navier-Stokes Equations," *AIAA 87-1107*, June 1987.
- [37] Abbot, I., and von Dönhoff, A.E., *Theory of Wing Sections*, Dover Publications Inc, New York, 1959.
- [38] Lighthill, M.J., *Laminar Boundary Layers*, (L. Rosenhead, ed.), Oxford Univ. Press, London and New York, 1963.
- [39] Perry, A.E., and Fairlie, B.D., "Critical Points in Flow Patterns," *Advances in Geophysics*, Vol 183, pp.299-315, 1974.
- [40] Peery, K.M., and Imlay, S.T., "Blunt-Body Flow Simulations," *AIAA 88-2904*, January 1988.
- [41] Liou, M.-S., and Steffen, C.J., "A New Flux Splitting Scheme," *NASA-TM-104404*, May 1991.

## Appendix:

### Preservation of Uniform Flow on an Arbitrary Mesh

*Claim:*  $\Delta U_{Visc}$  remains identically zero on any arbitrary, nonoverlapping hexahedral mesh when no spatial gradients are present in the state vector.

*Proof:* Let  $G$  be a 3D spatial graph with a hexahedral based tessellation containing node  $i$ . Taking the surface vectors of the polyhedra as described in the text, the viscous update to node  $i$  becomes (Eq. {11}):

$$\begin{aligned} (\bar{U}_{Visc})_i = \frac{\Delta t_i}{V_i} [ & \bar{\bar{F}}_V^N \cdot \bar{S}^N - \bar{\bar{F}}_V^S \cdot \bar{S}^S + \bar{\bar{F}}_V^E \cdot \bar{S}^E - \bar{\bar{F}}_V^W \cdot \bar{S}^W \\ & + \bar{\bar{F}}_V^F \cdot \bar{S}^F - \bar{\bar{F}}_V^B \cdot \bar{S}^B ] \end{aligned} \quad \{A.1\}$$

For the Navier-Stokes equations under the assumptions stated in the text,  $(\bar{\bar{F}}_V)^{N,S,E,W,F,B}$  are linear combinations of the first derivative quantities  $d_\xi \phi_\eta$  (Eq. {12}). Thus, when all  $d_\xi \phi_\eta = 0$  then the viscous fluxes  $(\bar{\bar{F}}_V)^{N,S,E,W,F,B} = 0$  (see Eqs. {3}-{7}) and  $\Delta U_{Visc}$  will vanish by Eq. {A.1}.

Referring to Figs. 2, 3, and 4, we begin by examining the members of the tensor  $d_{\xi}\phi_{\eta}$  along edge  $\bar{ij}$  which passes through the  $E$  face of the auxiliary cell surrounding node  $i$ .

$$\begin{aligned} (d_{\xi}\phi_{\eta})_i = \frac{1}{2} \frac{1}{V_i} & \left[ +\phi_{\eta}^j (S_{\xi_j^E} + S_{\xi_j^W}) - \phi_{\eta}^i (S_{\xi_i^E} + S_{\xi_i^W}) \right. \\ & + \phi_{\eta}^{n\alpha} (S_{\xi_i^N} + S_{\xi_j^N}) - \phi_{\eta}^{se} (S_{\xi_i^S} + S_{\xi_j^S}) \\ & \left. + \phi_{\eta}^{fe} (S_{\xi_i^F} + S_{\xi_j^F}) - \phi_{\eta}^{be} (S_{\xi_i^B} + S_{\xi_j^B}) \right] \end{aligned} \quad (A.3)$$

In a zero gradient field, however,  $\phi_{\eta}$  are constant at their reference ( $\infty$ ) values.

$$\begin{aligned} (d_{\xi}\phi_{\eta})_i = \frac{1}{2} \frac{\phi_{\eta}^{\infty}}{V_i} & \left[ + (S_{\xi_j^E} + S_{\xi_j^W}) - (S_{\xi_i^E} + S_{\xi_i^W}) \right. \\ & + (S_{\xi_i^N} + S_{\xi_j^N}) - (S_{\xi_i^S} + S_{\xi_j^S}) \\ & \left. + (S_{\xi_i^F} + S_{\xi_j^F}) - (S_{\xi_i^B} + S_{\xi_j^B}) \right] \end{aligned} \quad (A.4)$$

Thus, for the elements of  $d_{\xi}\phi_{\eta}$  to be zero, the bracketed term in (A.4) must sum to zero. This expression is exactly the sum of the surface vectors of the secondary cells. Rearranging the bracket in this expression, we seek to evaluate:

$$\begin{aligned} & \left[ +S_{\xi_j^E} + S_{\xi_j^W} - S_{\xi_i^E} - S_{\xi_i^W} + S_{\xi_i^N} + S_{\xi_j^N} \right. \\ & \left. - S_{\xi_i^S} - S_{\xi_j^S} + S_{\xi_i^F} + S_{\xi_j^F} - S_{\xi_i^B} - S_{\xi_j^B} \right] \end{aligned}$$

Collecting terms yields:

$$\begin{aligned} & \left[ +S_{\xi_j^W} - S_{\xi_i^W} + S_{\xi_i^N} - S_{\xi_i^S} + S_{\xi_i^F} - S_{\xi_i^B} \right. \\ & \left. + S_{\xi_j^E} - S_{\xi_i^E} + S_{\xi_j^N} - S_{\xi_j^S} + S_{\xi_j^F} - S_{\xi_j^B} \right] \end{aligned} \quad (A.5)$$

but  $S_{\xi_j^W} = S_{\xi_i^E}$  because it is the common face between auxiliary cells  $i$  and  $j$  and the expression in (A.5) may be re-written as:

$$\begin{aligned} & \left[ +S_{\xi_i^E} - S_{\xi_i^W} + S_{\xi_i^N} - S_{\xi_i^S} + S_{\xi_i^F} - S_{\xi_i^B} \right. \\ & \left. + S_{\xi_j^E} - S_{\xi_j^W} + S_{\xi_j^N} - S_{\xi_j^S} + S_{\xi_j^F} - S_{\xi_j^B} \right] \end{aligned} \quad (A.6)$$

We note that when the auxiliary cells are constructed as described in the text, they form a dual mesh consisting of closed volumes which fill the interior space of the graph without overlapping

or interior voids. Since the auxiliary cells are all closed volumes, their surface vectors sum to zero, and we have:

$$\begin{aligned} S_{\xi_i}^E - S_{\xi_i}^W + S_{\xi_i}^N - S_{\xi_i}^S + S_{\xi_i}^F - S_{\xi_i}^B &= 0 \\ S_{\xi_j}^E - S_{\xi_j}^W + S_{\xi_j}^N - S_{\xi_j}^S + S_{\xi_j}^F - S_{\xi_j}^B &= 0 \end{aligned} \quad \text{(A.7)}$$

Expression (A.6) then becomes identically zero, which ensures that the sum of surface vectors in Eq.(A.4) will always be zero. Thus, in accordance with the statements following Eq.(A.1),  $\Delta U_{visc}$  will always be identically zero in the presence of an unperturbed free stream flow.